



141
835
THS

**MATERIAL PROPERTY DOCUMENTATION AND FRACTURE
ANALYSES OF THE DEVELOPING SKULL**

By

Timothy G. Baumer

A THESIS

Submitted to
Michigan State University
in partial fulfillment of the requirements
for the degree of

MASTER OF SCIENCE

Engineering Mechanics

2009

ABSTRACT

MATERIAL PROPERTY DOCUMENTATION AND FRACTURE ANALYSES OF THE DEVELOPING SKULL

By

Timothy G. Baumer

Skull fracture interpretation is a necessary component of forensic analysis and contributes to the determination of the cause and manner of injury or death. The research presented in this thesis makes use of an *in situ* porcine model and finite element analysis to examine the responses of the developing skull to blunt force impulse and quasi-static crushing trauma. Chapter 2 documents age effects on the mechanical properties of parietal bone and coronal suture in porcine infants and correlates the bending properties of the bone to existing human infant data. Chapter 3 documents skull fracture on infant porcine specimens with respect to age and interface in an effort to identify fracture characteristics for a developing skull under known conditions. Chapter 4 uses a simplified cranial model and the finite element method to generate representative patterns of principal stress and strain directions developed during quasi-static crushing injuries to the developing skull. The theoretical results were compared to four clinical cases of known childhood fatalities from crushing head injuries inflicted by vehicle tires. Chapter 5 uses a simplified porcine cranial model and the finite element method to predict experimentally documented fracture patterns developed during impact loading to the parietal bone. The material properties of the cranial model were taken from the previously obtained results from Chapter 2. The experimentally inflicted fractures to the cranium from Chapter 3 were used for comparison with the theoretically developed principal stress and strain directions.

ACKNOWLEDGMENTS

I would like to thank my advisor and mentor, Dr. Roger Haut, for all his support and guidance over the past 4 years. I am also grateful to Dr. Todd Fenton for all his support and willingness to teach anthropology to an engineer. I would also like to thank all the members of the 4th floor of East Fee Hall for their friendship and support. I am grateful to Jean Atkinson, Jane Walsh, and Cliff Beckett for their continual technical support. Finally, I would like to acknowledge the contributions of Mr. Ed Reed and Ms. Star Lewis for supplying and collecting the porcine specimens.

TABLE OF CONTENTS

LIST OF TABLES	vi
LIST OF FIGURES.....	vii
RESEARCH PUBLICATIONS	x
CHAPTER 1: Characteristics of the Developing Skull – An Introduction.....	1
CHAPTER 2: Age-Dependent Mechanical Properties of the Infant Porcine	
Parietal Bone and a Correlation to the Human.....	10
Abstract	10
Introduction	12
Materials and Methods	14
Results	18
Discussion	23
References	28
CHAPTER 3: Age-Dependent Fracture Characteristics of Rigid and Compliant	
Surface Impacts on the Infant Skull – A Porcine Model.....	30
Abstract	30
Introduction	32
Materials and Methods	34
Results	38
Discussion	42
References	47
CHAPTER 4: Characteristics and Prediction of Cranial Crush Injuries in Children.....	50
Abstract	50
Introduction	52
Materials and Methods	54
Results	56
Discussion	61
References	65
CHAPTER 5: Finite Element Modeling of Rigid and Compliant Surface Impacts	
to the Pediatric Porcine Parietal Bone.....	66
Abstract	66
Introduction	68
Materials and Methods	70
Results	72
Discussion	74
References	78
CHAPTER 6: Conclusions and Recommendations for Future Work	80

APPENDIX A	83
APPENDIX B.....	94

LIST OF TABLES

Table 5.1. (Average) properties used in development of the FE model and impact conditions.	71
Table A.1. Raw data collected from 4-point bending tests of bone-suture-bone specimens	84
Table A.2. Raw data collected from 4-point bending tests of perpendicular bone specimens	86
Table A.3. Raw data collected from 4-point bending tests of parallel bone specimens	88
Table A.4. Raw data collected from 4-point bending tests of bone-suture-bone specimens NOT resulting in suture failure.....	90
Table A.5. Raw data collected from 4-point bending tests for multiple bone-suture-bone specimens taken from the same cranium.....	91
Table A.6. Porosity data from stained cross-sections of perpendicular bone specimens	92
Table A.7. Porosity data from stained cross-sections of parallel bone specimens.....	93
Table B.1. Raw data collected from rigid interface impacts	95
Table B.2. Skull damage measurements for rigid interface impacts.....	97
Table B.3. Raw data collected from compliant (1.1 MPa Hexcel) interface impacts	98
Table B.4. Skull damage measurements for compliant interface impacts	100

LIST OF FIGURES

Figure 1.1. Diagram of a newborn skull.....	2
Figure 2.1. Top view of cranium with locations of the beam specimens.....	15
Figure 2.2. Diagram of testing fixture.....	16
Figure 2.3. Representative stained cross-section of a beam from a 14 day specimen showing separation of compact and porous layers. Voids in the bone matrix were colored black. The box represents the analyzed area of a test specimen.....	18
Figure 2.4. Recorded values of stiffness for (a) both orientations of bone and (b) bone-suture-bone specimens from 3 to 21 days. *Significantly different means	19
Figure 2.5. Linear regressions of ultimate stress for bone and bone-suture-bone specimens against age	20
Figure 2.6. Ultimate strain for bone and bone-suture-bone specimens. *Significantly different means	20
Figure 2.7. Bending modulus for bone and bone-suture-bone specimens versus age. *Significantly different means.....	21
Figure 2.8. Strain energy of bone and bone-suture bone specimens versus age. *Significantly different means	22
Figure 2.9. Linear regression analyses of both orientations of infant porcine bone specimens against age. Both orientations displayed significant dependencies on age.....	22
Figure 2.10. Bending rigidity of human and porcine specimens versus age (Human – months; porcine – days). The human data was based on data from Coats and Margulies (2006) and unpublished data from Li et al (2007)	24
Figure 3.1. Skull positioning and set-up showing rigid impact head.....	35
Figure 3.2. Drop test fixture set-up	36
Figure 3.3. Overlay of force-time plots showing typical characteristics of an impact that caused fracture and one that did not	38
Figure 3.4. Peak force during impact for rigid and compliant interfaces.....	39

Figure 3.5. Contact area recorded on pressure sensitive film during impacts for rigid and compliant interfaces	39
Figure 3.6. Representative fracture sites for (a) rigid and (b) compliant interface impacts (five-day-old specimens shown). Fracture sites initiated at bone-suture boundaries. Compliant interface impact showed increased fracture lengths at similar initiation sites as the rigid interface impacts as well as diastatic fracture of coronal suture.....	40
Figure 3.7. Frequency of diastatic fractures caused by both rigid and compliant interfaces versus age.....	41
Figure 3.8. (Average) Fracture length generated by rigid and compliant impacts at the same impact energy	42
Figure 4.1. Simplified cranial model showing modeled landmarks of the basicranium. View of endocranial surface with vault removed	55
Figure 4.2. Diagrams of fractures due to quasi-static crushing forces to skulls aged (a) 5 years – Case 1, (b) 6 years – Case 2, (c) 3 years – Case 3, and (d) 1.5 years – Case 4. White cranial margins represent contact of applied forces (ground and tire)	58
Figure 4.3. (Case 1) Crushing injury to the skull of a 5-year-old. Diagrams of (a) clinically observed fractures and (b) an overlay of the highest 20% of principal tensile stresses produced from a FE model. White cranial margins represent contact of applied forces (ground and tire).....	59
Figure 4.4. (Case 2) Crushing injury to the skull of a 6-year-old. Diagrams of (a) clinically observed fractures and (b) an overlay of the highest 20% of principal tensile stresses produced from a FE model. White cranial margins represent contact of applied forces (ground and tire).....	60
Figure 4.5. (Case 3) Crushing injury to the skull of a 3-year-old. Diagrams of (a) clinically observed fractures and (b) an overlay of the highest 20% of principal tensile stresses produced from a FE model. White cranial margins represent contact of applied forces (ground and tire).....	60
Figure 4.6. (Case 4) Crushing injury to the skull of a 1.5 year old. Diagrams of (a) clinically observed fractures and (b) an overlay of the highest 20% of principal tensile stresses produced from a FE model. White cranial margins represent contact of applied forces (ground and tire).....	61
Figure 5.1. Simplified cranial model with overlays of modeled structures on true structures. Coronal cut of CT used for thickness comparison. *Feature	

not modeled. †Feature simplified. #Suture width altered for consistency with material property data obtained previously. Dotted line represents location of frontal bone removal 71

Figure 5.2. Overlay of maximum principal tensile stresses from FE models on representative experimental cranial fractures for (a) rigid interface impact to a young specimen, (b) rigid interface impact to an old specimen, (c) compliant interface impact to a young specimen, and (d) compliant interface impact to an old specimen. Longer lines represent higher stresses..... 73

Figure 5.3. Overlay of maximum principal tensile strains from FE models on representative experimental cranial fractures for (a) rigid interface impact to a young specimen, (b) rigid interface impact to an old specimen, (c) compliant interface impact to a young specimen, and (d) compliant interface impact to an old specimen. Longer lines represent higher strains 74

RESEARCH PUBLICATIONS

PEER-REVIEWED MANUSCRIPTS

Baumer T, Nashelsky M, Hurst C, Passalacqua N, Fenton T, and Haut R. Characteristics and Prediction of Cranial Crush Injuries in Children (in review)

Baumer T, Passalacqua N, Powell J, Newberry W, Smith W, Fenton T, and Haut R. Age-Dependent Fracture Characteristics of Rigid and Compliant Surface Impacts on the Infant Skull – A Porcine Model. *J. Forensic Sciences*. 2009 (in press)

Baumer T, Powell B, Fenton T, and Haut R. Age Dependent Mechanical Properties of the Infant Porcine Skull and a Correlation to the Human. *J Biomechanical Eng*. 2009 (in press)

Meyer E, Baumer T, Slade J, Smith W, Haut R. Tibiofemoral contact pressures and osteochondral microtrauma during ACL rupture due to excessive compressive loading and internal torque of the human knee. *Am J Sports Med*. 2008; doi: 10.1177/0363546508318046

PEER-REVIEWED ABSTRACTS

Baumer TG, Powell BJ, Fenton TW, Haut RC. Age Dependent Mechanical Properties of the Infant Porcine Skull and a Correlation to the Human. *Am. Society of Mechanical Engineering, Lake Tahoe, CA, 2009.*

Fenton TW, Passalacqua NV, Baumer TG, Powell BJ, Haut RC. A Forensic Pathology Tool to Predict Pediatric Skull Fracture Patterns - Part 1: Investigations on Infant Cranial Bone Fracture Initiation and Interface Dependent Fracture Patterns. *Am. Academy of Forensic Sciences (AAFS), Denver, Colorado, 2009. [Winner of the Ellis R. Kerley Award]*

Nashelsky MB, Fenton TW, Passalacqua NV, Hurst CV, Baumer TG, Haut RC. Cranial Fracture Patterns in Pediatric “Crushing” Injuries and Preliminary Biomechanical Modeling Using a Simple Finite Element Model. *AAFS, Denver CO, 2009.*

Meyer EG, Baumer TG, Haut RC. Knee joint relative motion during ACL rupture by internal tibial torsion of tibiofemoral compression. *North Am. Congress on Biomechanics (NACOB), Ann Arbor, Michigan, 2008.*

Meyer EG, Baumer TG, Haut RC. Tibiofemoral contact pressures and osteochondral microtrauma from ACL rupture via hyperextension and joint compression. *NACOB, Ann Arbor, MI, 2008.*

Meyer EG, Baumer TG, Haut RC. Tibiofemoral contact pressures and osteochondral microtrauma during ACL rupture due to excessive compressive loading and internal tibial torsion. *NACOB, Ann Arbor, MI, 2008.*

CHAPTER ONE

CHARACTERISTICS OF THE DEVELOPING SKULL – AN INTRODUCTION

Skeletal fractures are diagnosed in nearly 1 of 3 children investigated for physical abuse with eighty percent of all fractures from abuse occurring in children less than 18 months of age (Belfer et al, 2001). Head injuries account for 80% of fatal child abuse (Case et al, 2001), while short falls rarely, if ever, cause serious injury or death (Reiber, 1993). However, non-fatal injury from short falls (less than 3 feet) can still result in skull fracture especially for infants less than 12 months of age (Gruskin and Schutzman, 1999). Distinguishing between abuse and accidental trauma can be very difficult since both types of trauma may produce similar types of injuries (Billmire and Myers, 1985). Specifically, linear, complex, and depressed fractures can be seen in both types of cases (Reece and Sege, 2000; Wheeler and Shope, 1997). Some attempts have been made to create a model of the developing skull, but data are limited. One modeling effort involves scaling of the adult skull, which has met with some success in predicting impact response of the pediatric skull (Prange et al, 2004). However, the head of an infant is smaller and geometrically unlike that of an adult (Schneider et al, 1986) and the validity of predicting skull fracture patterns in infants from adult data has not been investigated.

Using adult data to predict skull fracture patterns in the pediatric skull may also be problematic due to the different structural (ease of deformation and decreased threshold to fracture) and mechanical properties of the infant skull (Thibault and Margulies, 1998; Prange et al, 2000; Prange and Margulies, 2002). The developing skull

consists of several bones joined by soft tissue (sutures) that allow growth of the cranium during childhood (Figure 1.1). These bones are developed during fetal life and grow rapidly over the first two years after birth, with decreasing growth rates into adulthood (Mertz, 1984). The anterior fontanelle closes between 9 and 26 weeks after birth, but is not sealed until around 18 months (Knight, 1991). In adulthood, the sutures of the skull ossify creating one solid structure, whereas the sutures of infants result in more isolated regions.

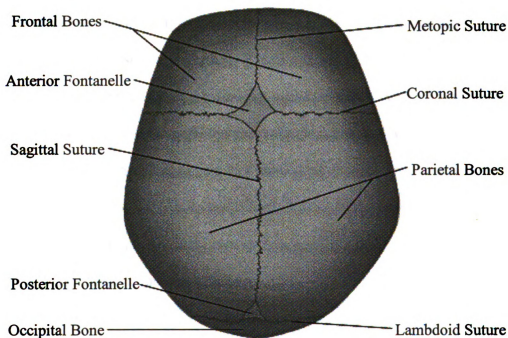


Figure 1.1. Diagram of a newborn skull.

While several studies have documented important information regarding the response of the infant skull and brain to blunt force impact, these data are limited to one or two age groups. And because of ethical considerations, experimentation on human pediatric specimens is very limited. However, one animal model of the human infant has begun to emerge regularly in the current literature. A study by Dickerson and Dobbing

(1967) shows a similarity in development of the central nervous system when correlating months of the human to weeks of the pig. Other studies have used porcine models to predict fracture loads for the infant human femur (Pierce et al., 2000) and strain in the braincase and sutures (Herring and Teng, 2000). An important finding in studies on the porcine infant cranial bone and suture is “that the elastic modulus, rupture modulus, and energy absorbed to failure of infant (2-3 day old) cranial (parietal) bone are similar to that of the human infant in three-point bending” (Margulies and Thibault, 2000).

While Margulies and Thibault (2000) have attempted to correlate the mechanical behavior of human infant cranial bone to porcine infant cranial bone, the ages and number of specimens tested were limited. The data shows a linear increase in mechanical properties with age, but includes prenatal and postnatal aged specimens. Since questions of abuse in the pediatric patient typically involve subjects up to 18 months of age, which correlates to a time of rapid skull growth, the biomechanical properties of developing skull bones and sutures must be well documented over this entire period of developmental time if an accurate age-dependent model is to be created. Yet, the age-dependent properties of the developing skull are not the only conditions affecting fracture patterns. The risk of injury is also dependent on the contacting surface and fall height (Bertocci et al., 2003; Chalmers et al., 1996). Other variables, such as the area struck, thickness of the skull, thickness of scalp and hair, and impact direction can also affect the fracture pattern (Knight, 1991; Cooperman and Merten, 2001). Head injuries are often the result of dynamic forces in which a moving object strikes the cranium at a considerable speed or the cranium makes contact with a static object that causes the skull to be rapidly decelerated (Duhaime et al., 1995). However, cases of

crushing injuries, where a static load is applied relatively slowly to the cranium, are also present in the literature. Unfortunately, due to the paucity of skull fracture tolerance data for infants and young children, pediatric trauma involving single-event head injuries with related cranial fractures represent one of the greatest challenges to forensic pathologists and anthropologists. Since it is often the job of the forensic professional to try to recognize characteristic patterns in these cases, a clear understanding of fracture propagation, and the effects of the aforementioned variables, becomes vital.

Studies involving impact loading of the cranium have been presented, but there are also several case reports of basilar skull damage in the literature involving both crushing and impulse based loading scenarios mainly focusing on adult crania. A study involving 15 cases of crushing injuries to adult skulls aged 14-63 years and experimentally induced fractures on 11 cadaver crania revealed similarities in basilar fracture patterns (Russell and Schiller 1949). However, a study by Harvey and Jones (1979) claimed that fractures through both petrous bones was not an indicator of impact site. Another study by Yasue (1981) then suggested that the overall path of fracture through the basicranium could, in fact, be related to the region of the skull impacted. While it is assumed that fractures will generally follow the path of least resistance, this path may be different between the child and adult cranium. While all of these aforementioned studies focused on adult crania, some recent case reports on quasi-static loading to the crania of children have also presented observations of basilar fractures (Takeshi, 2005; Duhaime et al., 1995). The trend of quasi-static loading producing basilar fractures in both adults and children may suggest that prediction of these fractures is possible.

Theoretical techniques are widely used for prediction of material failure in structures. The Finite Element (FE) method is a powerful analytical modeling tool that can be used to determine internal stresses and strains within a complex solid. Several studies have shown that maximum principal stress (or strain) directions from a modeled structure correlate well with areas of experimentally or clinically observed bone fractures (Graham 2000; Silva 1998; Doorly 2006). While modeling of fracture propagation generally involves high computational costs, one theory suggests that there is a close, although not exact, relationship between pre-failure stress trajectories and the ultimate path of propagation. In brief, Frank and Lawn (1967) proposed that crack growth occurs in such a way as to maximize the energy dissipation per unit length of growth, and that the greatest amount of dissipation occurs when the crack plane is perpendicular to the direction of greatest principal tensile stress. In other words, the directions of principal tensile stress developed on a solid may be a reasonable predictor of propagation direction.

Skull fracture interpretation is a necessary component of forensic analysis and contributes to the determination of the cause and manner of injury or death. The research presented in this thesis makes use of an *in situ* porcine model and finite element analysis to examine the responses of the developing skull to blunt force impulse and quasi-static crushing trauma. Chapter 2 documents age effects on the mechanical properties of parietal bone and coronal suture in porcine infants and correlates the bending properties of the bone to existing human infant data. Chapter 3 documents skull fracture on infant porcine specimens with respect to age and interface in an effort to identify fracture characteristics for a developing skull under known conditions. This study hypothesized

that impact energy required to initiate a skull fracture would depend on specimen age, and the extent of fracture damage for a given energy impact would depend on impact interface. Chapter 4 uses a simplified cranial model and the finite element method to develop representative patterns of principal stress and strain directions developed during quasi-static crushing injuries to the developing skull. The theoretical results were compared to four clinical cases of known childhood fatalities from crushing head injuries inflicted by vehicle tires. Chapter 5 uses a simplified porcine cranial model and the finite element method to predict experimentally documented fracture patterns developed during impact loading to the parietal bone. The material properties of the cranial model were taken from the previously obtained results from Chapter 2. The experimentally inflicted fractures to the cranium from Chapter 3 were used for comparison with the theoretically developed principal stress and strain directions.

The research presented in this thesis provides useful data in regards to the material properties of the developing porcine skull, and has suggested a correlation with the developing human skull. This research also documents fractures generated on the developing skull due to blunt force trauma with respect to age and interface. The experimentally and clinically observed fractures were predicted using a simplified theoretical model of impact and quasi-static loading of the cranium. This information may prove relevant in determining perimortem events in forensic cases of pediatric cranial injuries with unknown or questionable circumstances. These data may have ultimate utility in the study of potential child abuse cases.

REFERENCES

- Belfer R, Klein B, and Orr L., 2001, "Use of the Skeletal Survey in the Evaluation of Child Maltreatment," *American Journal of Emergency Medicine*, **19**, pp. 122-4.
- Bertocci G. and Pierce M., 2006, "Applications of Biomechanics Aiding in the Diagnosis of Child Abuse," *Clinical Pediatric Emergency Medicine*, **7**, pp. 194-9.
- Billmire M. and Myers P., 1985, "Serious head injury in infants: accident or abuse?," *The American Academy of Pediatrics*, **75**, pp. 340-2.
- Case M, Graham M, Handy T, Jentzen J, Monteleone J., 2001, "Position Paper on Fatal Abusive Head Injuries in Infants and Young Children," *The American Journal of Forensic Medicine and Pathology*, **22**, pp. 112-22.
- Chalmers D, Marshall S, Langley J, Evans M, Brunton C, Kelly A, et al., 1996, "Height and surfacing as risk factors for injury in falls from playground equipment: a case-control study," *Injury Prevention*, **2**, pp. 98-104
- Cooperman D. and Merten D., 2001, "Skeletal Manifestation of Child Abuse," In: *Child Abuse: Medical Diagnosis and Management*. Philadelphia: Lippincott, Williams, and Wilkins, pp. 123-56.
- Dickerson J. and Dobbing J., 1967, "Prenatal and postnatal growth and development of the central nervous system of the pig," *Proceedings of the Royal Society of London*, **166(1005)**, pp. 384-95.
- Doorly M, Gilchrist M., 2006, "The use of accident reconstruction for the analysis of traumatic brain injury due to head impacts arising from falls," *Computer Methods in Biomechanics and Biomedical Engineering*, **9(6)**, pp. 371-7.
- Duhaime A-C, Eppley M, Margulies S, Heher K, Bartlett S., 1995, "Crush Injuries to the Head in Children," *Neurosurgery*, **37(3)**, pp. 401-7.
- Frank F, Lawn B., 1967, "On the Theory of Hertzian Fracture," *Proceedings of the Royal Society of London*, **299(1458)**, pp. 291-306.
- Graham R, Oberlander E, Stewart J, Griffiths D., 2000, "Validation and use of a finite element model of C-2 for determination of stress and fracture patterns of anterior odontoid loads," *Journal of Neurosurgery (Spine 1)*, **93**, pp. 117-25.
- Gruskin K. and Schutzman S., 1999, "Head Trauma in Children Younger Than 2 Years," *Archives of Pediatric Adolescent Medicine*, **153**, pp.15-21.

Harvey F, Jones A., 1980, "'Typical' Basal Skull Fracture of Both Petrous Bones: An Unreliable Indicator of Head Impact Site," *Journal of Forensic Sciences*, **25(2)**, pp. 280-6.

Herring S. and Teng S., 2000, "Strain in the Braincase and Its Sutures During Function," *American Journal of Physical Anthropology*, **112**, pp. 575-593.

Knight B., 1991, "Fatal child abuse," In: *Forensic Pathology*. London: Edward Arnold, pp. 457-73.

Mertz H., 1984, "A Procedure for Normalizing Impact Response Data," SAE #840884, 29th Stapp Car Crash Conference, Chicago, IL.

Pierce M, Valdevit A, Anderson L, Inoue N, and Hauser D., 2000, "Biomechanical Evaluation of Dual-Energy X-Ray Absorptiometry for Predicting Fracture Loads of the Infant Femur for Injury Investigation: An In Vitro Porcine Model," *Journal of Orthopaedic Trauma*, **14(8)**, pp. 571-6.

Prange M, Luck J, Dibb A, Van Ee C, Nightingale R, Myers B., 2004, "Mechanical Properties and Anthropometry of the Human Infant Head," *Stapp Car Crash Journal*, **48**, pp. 279-99.

Prange M, Meaney D, Margulies S., 2000, "Defining brain mechanical properties: Effects of region, direction, and species," *Stapp Car Crash Journal*, **44**, pp. 205-213.

Prange M. and Margulies S., 2002, "Regional, Directional, and Age-Dependant Properties of the Brain Undergoing Large Deformations," *Journal of Biomechanical Engineering*, **124(2)**, pp. 244-52.

Reece R and Sege R., 2000, "Childhood Head Injuries: Accidental or Inflicted," *Archives of Pediatric Adolescent Medicine*, **154**, pp. 11-15.

Reiber G., 1993, "Fatal falls in childhood: How Far Must Children Fall to Sustain Fatal Head Injury?," *American Journal of Forensic Medicine and Pathology*, **14**, pp. 201-7.

Russell W, Schiller F., 1949, "Crushing Injuries to the Skull: Clinical and Experimental Observations," *Journal of Neurology, Neurosurgery, and Psychiatry*, **12**, pp. 52-60.

Schneider L, Lehman R, Pflug M, Owings C., 1986, "Size and Shape of the Head and Neck From Birth to Four Years," Washington, D.C. The Consumer Product Safety Commission, Report No.: UMTRI-86-2.

Silva M, Keaveny T, Hayes W., 1998, "Computed Tomography-Based Finite Element Analysis Predicts Failure Loads and Fracture Patterns for Vertebral Sections," *Journal of Orthopaedic Research*, **16**, pp. 300-8.

Takeshi M, Okuchi K, Nishiguchi T, Seki T, Watanabe T, Ito S, et al., 2006, "Clinical Analysis of Seven Patients of Crushing Head Injury," *The Journal of Trauma-Injury, Infection, and Critical Care*, **60(6)**, pp. 1245-9.

Thibault K. and Margulies S., 1998, "Age-Dependant Material Properties of the Porcine Cerebrum: Effect on Pediatric Head Injury Criteria," *Journal of Biomechanics*, **31(12)**, pp. 1119-26.

Wheeler D. and Shope T., 1997, "Depressed skull fracture in a 7-month old who fell from bed," *Pediatrics*, **100**, pp. 1033-4.

Yasue M., 1981, "Clinical and experimental investigation of mediobasal skull fracture," *Neurol Med Chir (Tokyo)*, **21**, pp. 1041-9.

CHAPTER TWO

AGE DEPENDENT MECHANICAL PROPERTIES OF THE INFANT PORCINE PARIETAL BONE AND A CORRELATION TO THE HUMAN

ABSTRACT

An infant less than 18 months of age with a skull fracture has a 1 in 3 chance of abuse. Injury biomechanics are often used in the investigation of these cases. In addition to case-based investigations, computer modeling, and test dummies, animal model studies can aid in these investigations. This study documents age effects on the mechanical properties of parietal bone and coronal suture in porcine infants and correlates the bending properties of the bone to existing human infant data. Three beam specimens were cut from porcine specimens aged 3, 7, 10, 14, 18, and 21 days: one across the coronal suture and two from the parietal bone, one parallel to and one perpendicular to the coronal suture. An actuator-mounted probe applied 4-point bending in displacement control at 25mm/sec until failure. Bending stiffness of bone specimens increased with age; bone-suture-bone specimens showed no change up to 14 days, but increased from 14 to 18 days. All three specimen types showed decreases in ultimate stress with age. Ultimate strain for the bone-suture-bone specimens was significantly higher than that for the bone specimens up to 14 days, with no differences thereafter. There was no change in the bending modulus with age for any specimen type. Bone-suture-bone bending modulus was lower than that of the bone specimens up to 14 days, with no differences thereafter. There was no change in strain energy to failure with age for the bone specimens; bone-suture-bone specimens showed no change up to 14 days, but decreased from 14 to 18 days. There was an increase in specimen porosity with age. Correlation

analysis revealed a weak (-0.39), but significant, negative correlation between ultimate stress and porosity. While the mechanical properties of parietal bone and coronal suture did not change significantly with age, bone specimens showed an increase in bending stiffness with age. Bone-suture-bone specimens showed an increase in bending stiffness only between 14 and 18 days of age. Correlation analyses using existing and new data to compute the bending rigidity of infant parietal bone specimens suggested that days of pig age may correlate with months of human age during the most common time frame of childhood abuse cases. Such a correlation may support the developing porcine model as an important biomechanical tool for the study of pediatric skull fracture in efforts to investigate cases of childhood abuse.

INTRODUCTION

Skeletal fractures are diagnosed in nearly 1 of 3 children investigated for physical abuse (Belfer et al., 2001). Often it is the job of the forensic anthropologist to try to recognize characteristic patterns in these cases, but in reality it is difficult to diagnose abuse simply based on a fracture. In fact, age together with the type and site of fracture are important features to consider when assessing cases of potential abuse (Kemp et al., 2008). Eighty percent of all fractures from abuse are seen in children less than 18 months of age. For these children the probability of abuse given a skull fracture, for example, is 0.30 (range 0.19 to 0.46). The most common site of skull fracture in abuse and non-abuse cases is the parietal bone (Meservy et al., 1987), with the most common fracture type being linear (Reece and Sege, 2000).

Injury biomechanics are often used in the investigation of cases suspected to involve child abuse (Bertocci and Pierce, 2006). In addition to case-based investigations, computer modeling, and the use of test dummies, animal model studies can aid in these investigations. While the relationship between animal studies and the human pediatric patient is yet unclear in most circumstances, one animal model seems to have regularly emerged in the current literature. For example, a study has been conducted on prediction of fracture loads for the infant femur using porcine models aged 3-12 months (Pierce et al., 2000). In another study on strain in the braincase and its sutures, juvenile pigs have again been used as a model of the human infant (Herring and Teng, 2007). Dickerson and Dobbing (1966) have previously compared the development of the porcine central nervous system to the human and found that months of life in the human are roughly comparable to weeks in a pig. An important finding in studies on the porcine infant

cranial bone and suture is “that the elastic modulus, rupture modulus, and energy absorbed to failure of infant (2-3 day old) cranial (parietal) bone are similar to that of the human infant in three-point bending” (Margulies and Thibault, 2000).

While Margulies and Thibault (2000) have attempted to correlate the mechanical behavior of human infant cranial bone to porcine infant cranial bone, the ages and number of specimens tested were limited. The data shows a linear increase in mechanical properties with age, but the data includes prenatal and postnatal aged specimens. Other studies have shown that growth of the human skull involves large increases in size over the first two years of life, with decreasing growth rates into adulthood (Mertz, 1984). Since questions of abuse in the pediatric patient typically involve subjects up to 18 months of age, an objective of the current study was to document the biomechanical properties of developing porcine skulls and sutures over a longer period of developmental time than previous studies.

Additionally, Margulies and colleagues have documented the biomechanical properties of the infant porcine parietal bone using beam specimens oriented perpendicular to and across the coronal suture, but case-based investigations show linear skull fractures in infants typically initiate at an ossification center and run parallel to and perpendicular to spiculae in the parietal bone (Holck, 2005). It has also been shown that the mechanical properties of prenatal human infant parietal bone is non-isotropic (McPherson and Kriewall, 1980). Therefore in the current study, beam specimens were taken from the developing porcine parietal bone both parallel and perpendicular to the coronal suture, as well as across it. The data from the current study will provide

information on the age factor for developing parietal bone and coronal suture in the porcine infant model, as it may relate to the human pediatric patient.

MATERIALS AND METHODS

Porcine specimens aged 3 days (n=5), 7 days (n=8), 10 days (n=7), 14 days (n=5), 18 days (n=5), and 21 days (n=4) were obtained from a local supplier and stored at -20°C until testing. All animals died of natural causes and the specimens were frozen within 12 hrs of death. None of the specimens had outward signs of head injury, which was later confirmed during specimen preparation.

Each specimen was thawed at room temperature for 24 hours prior to testing. The scalp was removed, but the periosteum was left intact to help prevent drying of the bone and sutures. The top palette of the skull was removed using a surgical saw (Autopsy Saw, Stryker, Kalamazoo, MI). Cuts were made at the lambdoid suture, along the lateral aspect of the parietal bone, and diagonally across the frontal bone from the lateral aspect of the coronal suture to an anterior location along the sagittal suture.

Three beam specimens were cut from each skull: one across the coronal suture and two from the parietal bone, one parallel to and one perpendicular to the coronal suture (Figure 2.1). The specimens were cut with a bone saw (Isomet 1000, Buehler, Lake Bluff, IL), while bathed in phosphate buffered saline (PBS). The specimen width varied from 4.5 to 5.5 mm wide. Due to the non-uniform thickness of the beam specimens, three thickness measurements were taken from each specimen at equally spaced intervals along the beam. These measurements were used to calculate an average thickness of each specimen. The length of the beam specimens was fixed at 15 mm to

yield a length to thickness ratio of approximately 8:1. The cut specimens were stored in room-temperature PBS for less than 1 hour before testing.

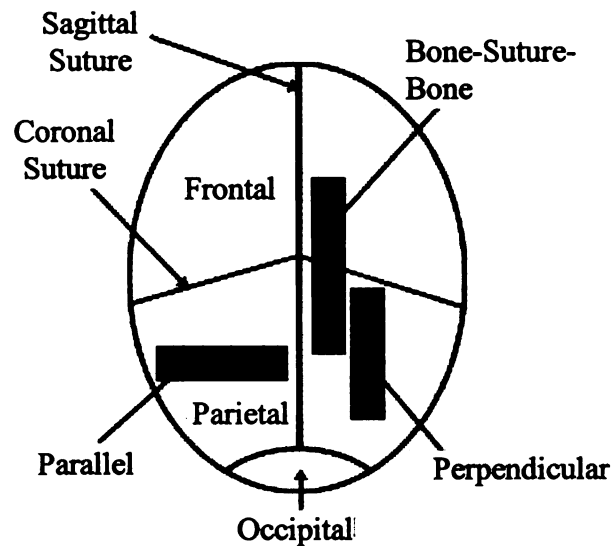


Figure 2.1. Top view of cranium with locations of the beam specimens.

The beam specimens were loaded to failure in 4-point bending. Each specimen was mounted between two aluminum sleeves using air-hardening cement (Technovit, Jorgensen Laboratories Inc., Loveland, CO). The fixed testing length of 15 mm was maintained with a thin aluminum bar fastened between the sleeves. This bar also served to prevent damage to the specimen during preparation and mounting in the test fixture.

The potted specimens were mounted in a custom-designed 4-point bending fixture (Figure 2.2) attached to a servo-hydraulic testing machine (Model 1331, Instron Corp., Canton, OH). One end of the fixture was mounted on linear bearings to allow displacement along the specimen axis. An actuator-mounted probe was located on each of the two sleeves to apply 4-point bending. A 111.2-N load-cell (Model #JP25, Data Instruments Inc., Acton, MA) was mounted between the probe and actuator. The experiments were run with the machine in displacement control at 25mm/sec to generate the bending moment on the beam specimens.

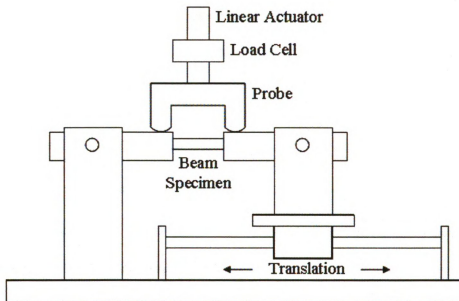


Figure 2.2. Diagram of testing fixture.

The force and actuator displacement were recorded to failure during each experiment. From these values, initial specimen stiffness, ultimate stress (σ_{ult}), ultimate strain (ϵ_{ult}), bending modulus (E), and strain energy to failure (U) were determined using the following information. Initial stiffness was calculated from the initial linear portion of the force-actuator displacement plot. Ultimate stress at the endocranial surface was determined from simple beam theory using

$$\sigma_{ult} = \frac{M^* y}{I_f} \quad (2.1)$$

where M^* was the bending moment at failure, y was the distance from the inner surface of the specimen to the centroidal axis, and I_f was the second moment of the rectangular area measured at the fracture location. Ultimate strain at the fracture location was calculated from

$$\epsilon = \frac{2y\alpha}{L} \quad (2.2)$$

where y was the distance from the inner surface of the specimen to the centroidal axis, α was the angular rotation of the beam under the probes at failure, and L was the length of the specimen. The elastic modulus was also determined from simple beam theory using

$$E = \frac{M}{\alpha} \frac{L}{2I_{avg}} \quad (2.3)$$

where M/α was the moment-angular rotation ratio during the initial linear region of the force-displacement trace, and I_{avg} was the second moment of area determined using the average thickness over the length of the beam specimen. The failure strain energy was then computed with the following integral equation

$$U = \int_0^L \frac{(M^*)^2}{2EI_{avg}} dx \quad (2.4)$$

where 'x' was the distance along the beam from the stationary aluminum cylinder.

The gross morphological features of the beams were documented by staining the length-wise cross-section of the failed specimens with India ink (Figure 2.3). Each test specimen was photographed with a digital camera mounted to a dissecting microscope at 50x magnification (Wild M5A, Wild Heerbrugg, Switzerland). A representative section of bone was cropped from the exocranium to the endocranium that included an equal distance along the length of the beam. This image was always taken in an area between characteristic undulations in the specimen thickness, as this was the area of failure during the experiments. The image was imported to an image analysis program (Sigma Scan, Jandel Scientific, San Rafael, CA) and converted to grayscale. The porosity was determined as the area of the stain (voids) per total area.

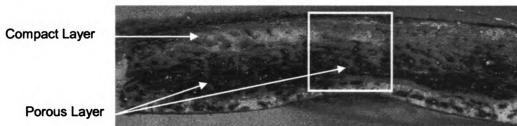


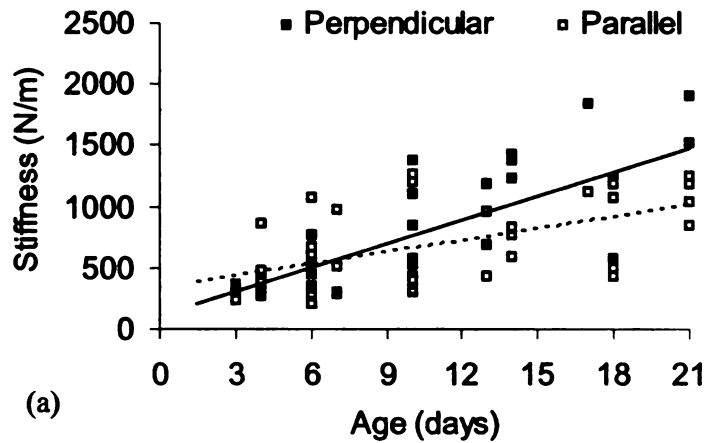
Figure 2.3. Representative stained cross-section of a beam from a 14 day specimen showing separation of compact and porous layers. Voids in the bone matrix were colored black. The box represents the analyzed area of a test specimen.

Each material property data set was analyzed for age effects using linear regression analyses. Comparisons between the three specimen types was performed using a two-factor (age, type) ANOVA. A Pearson Product Moment correlation was used to analyze the effect of porosity on ultimate stress. Statistically significant effects were reported for $p < 0.05$.

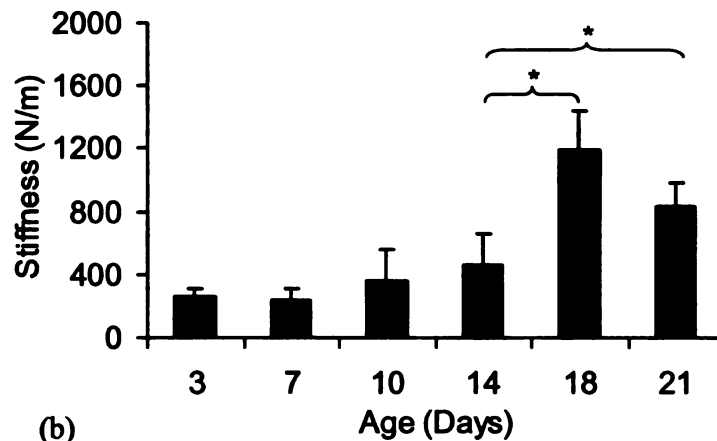
RESULTS

There was no difference in average thickness measurements between the bone and bone-suture-bone specimens for any age. Linear regression analyses also showed a significant increase in thickness with age ($p < 0.001$ for each specimen type).

For each orientation of parietal bone specimen, there was a significant increase in bending stiffness with age (Figure 2.4a). The slopes were not statistically dependent on orientation. Interestingly, there was no significant change in bending stiffness in the bone-suture-bone specimens up to fourteen days, but between fourteen and eighteen days there was a significant increase (Figure 2.4b). The stiffness of the suture was lower than that of the bone up to fourteen days, but it became statistically greater than the parallel bone specimens at eighteen days (suture 1197 ± 246 N/m; parallel 864 ± 367 N/m).



(a)



(b)

Figure 2.4. Recorded values of stiffness for (a) both orientations of bone and (b) bone-suture-bone specimens from 3 to 21 days. *Significantly different means.

All bone specimens failed at a thinned area and all bone-suture-bone specimens failed in the suture. Linear regression analyses showed significant decreases in ultimate stress for both orientations of bone ($p < 0.05$) and for the bone-suture-bone specimens ($p < 0.01$) with age (Figure 2.5). The slopes were not different.

There was no change with age in ultimate strain in the bone (0.0163 ± 0.0053 mm/mm) and bone-suture-bone (0.0313 ± 0.0072 mm/mm) specimens (Figure 2.6). The ultimate strain for the bone-suture-bone specimens was significantly higher than that for the bone specimens up to fourteen days.

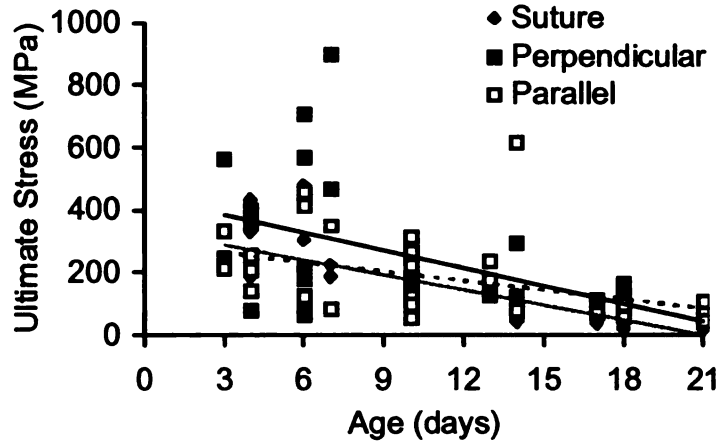


Figure 2.5. Linear regressions of ultimate stress for bone and bone-suture-bone specimens against age.

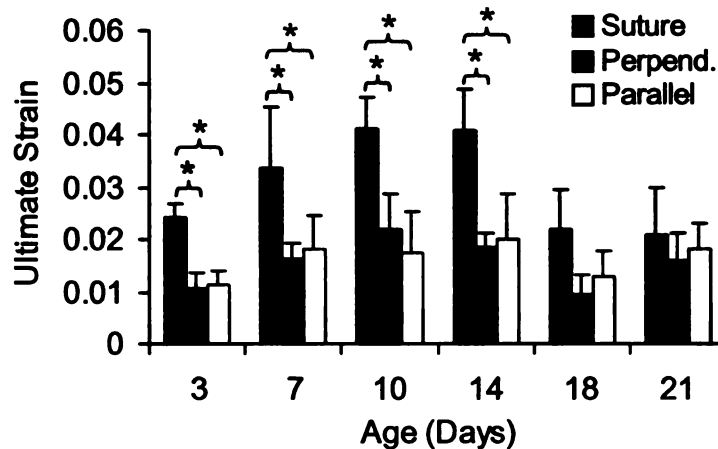


Figure 2.6. Ultimate strain for bone and bone-suture-bone specimens. *Significantly different means.

There was no change with age in the bending modulus of the bone (6.01 ± 1.73 GPa) and bone-suture-bone (2.73 ± 0.84 GPa) specimens (Figure 2.7). The bending modulus of the bone-suture-bone specimens was significantly lower than that of the bone specimens up to fourteen days.

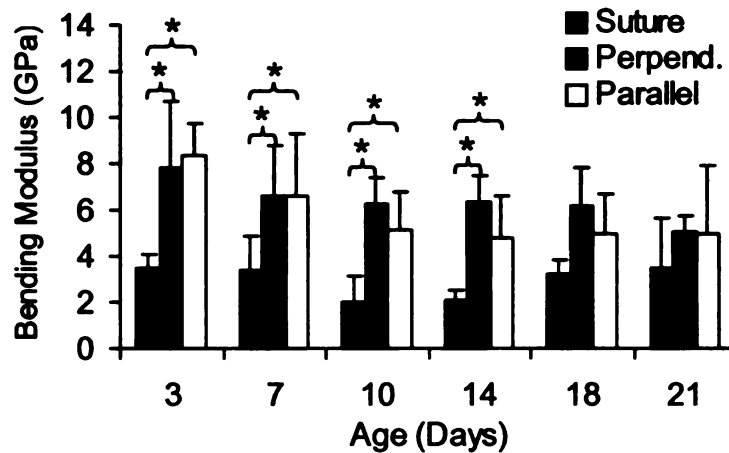


Figure 2.7. Bending modulus for bone and bone-suture-bone specimens versus age.

*Significantly different means.

There was also no change with age in the strain energy to failure for the bone specimens, being 0.03 ± 0.03 J and 0.03 ± 0.04 J for perpendicular and parallel orientations, respectively (Figure 2.8). The bone-suture-bone specimens showed no change up to fourteen days (0.23 ± 0.13 J). For ages up to fourteen days, the strain energy to failure of the bone-suture-bone specimens was significantly higher than that of the bone specimens. From fourteen to eighteen days, however, there was a significant decrease in the strain energy of the bone-suture-bone specimens. Therefore, the strain energy to failure was no longer different for the bone (0.01 ± 0.00 J) versus bone-suture-bone specimens (0.01 ± 0.00 J).

The morphological characteristics of the skull bone from the infant porcine specimens changed during the aging process. It was found that two distinct layers, one that was visually quite compact and another more porous layer, were present as early as three days. The porous layer appeared as pockets beneath the compact layer which

developed through ten days, and by fourteen days there was a clear separation of zones along the entire specimen (see Figure 2.3).

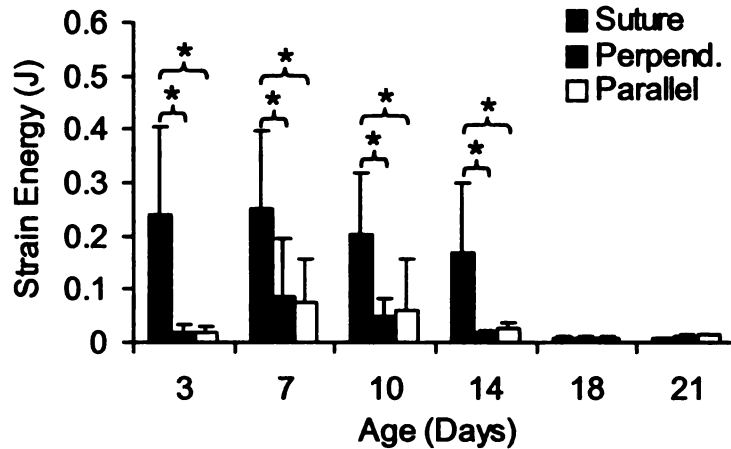


Figure 2.8. Strain energy of bone and bone-suture bone specimens versus age. *Significantly different means.

Analysis of both orientations of bone specimens revealed an increase in porosity with age ($p < 0.001$) (Figure 2.9). Correlation analysis of the combined data revealed a weak (-0.391), but significant ($p < 0.01$), negative correlation between ultimate stress and porosity. No other mechanical property had a significant correlation with porosity.

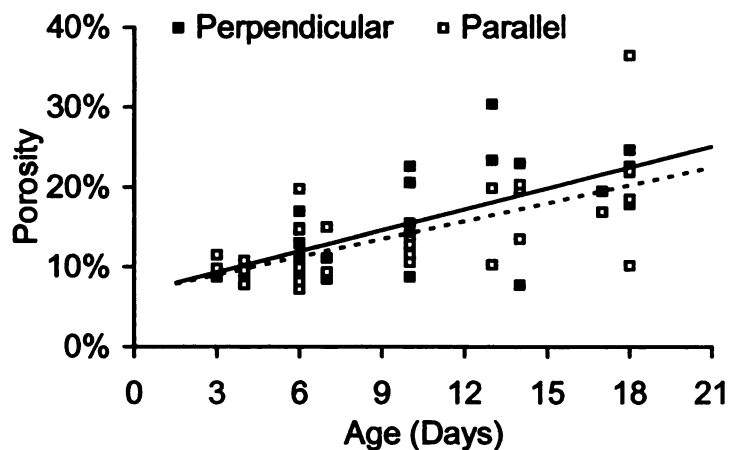


Figure 2.9. Linear regression analyses of both orientations of infant porcine bone specimens against age. Both orientations displayed significant dependencies on age.

DISCUSSION

The current study was performed to document potential changes in the mechanical properties of infant porcine parietal bone as a function of age. Linear regression analyses on the bending modulus of porcine specimens showed no significant change with age. A few previous studies on human specimens have shown a linear increase in the bending modulus of prenatal human infant parietal bone and it has been suggested that this trend may continue up to six months (Margulies and Thibault, 2000), or even six years (McPherson and Kriewall, 1980) of age. These studies, however, assumed a linear increase from the prenatal data to the older specimens and did not collect data between the endpoints. A study by Coats and Margulies (2006) investigates the mechanical properties of both prenatal and postnatal infants from twenty-six weeks of gestation to thirteen months of age. The authors claimed that there was a significant increase in bending modulus with age, but a closer inspection of their data indicated that the increase in these properties was significantly influenced by the prenatal data. When linear regression analysis was performed on the postnatal data alone there was no statistical change in bending modulus with age. These data are in agreement with the current study using infant porcine skull bone.

The bending modulus data from the human parietal bone of Coats and Margulies (2006) have also been compared to the bending modulus of the porcine parietal bone. It was clear that the porcine parietal bone bending modulus was significantly higher than that of the human parietal bone. However, this is a material rather than a structural parameter of comparison. Since the current thought was to use the porcine model to study issues of potential childhood abuse, a structural comparison may be more

appropriate. In this effort we were able to obtain unpublished human infant parietal bone thickness data for ages two to twenty-one months, $n=314$, from a recent study by Li et al. (2007). While the human skull was significantly thicker than the porcine skull over the ages studied here, a linear regression of parietal bone thickness versus age indicated growth rates of parietal bone thickness for humans to be 0.0487 mm/month and that of pigs to be 0.0492 mm/day. Using bending modulus data from Coats and Margulies (2006) and thickness values obtained during the Li et al. (2007) study, the bending rigidity of human infant parietal bone versus age in months was compared to that of the porcine specimens versus age in days (Figure 2.10). The slopes of parietal bone bending rigidity versus age were $0.505 \text{ GPa}\cdot\text{m}^4/\text{month}$ for humans and $0.596 \text{ GPa}\cdot\text{m}^4/\text{day}$ for the porcine specimens. The difference between human and porcine data may be due to differences in the strain rates of testing. The human specimens were tested at a high velocity (approximately 2 m/sec), while the porcine specimens were tested at a lower

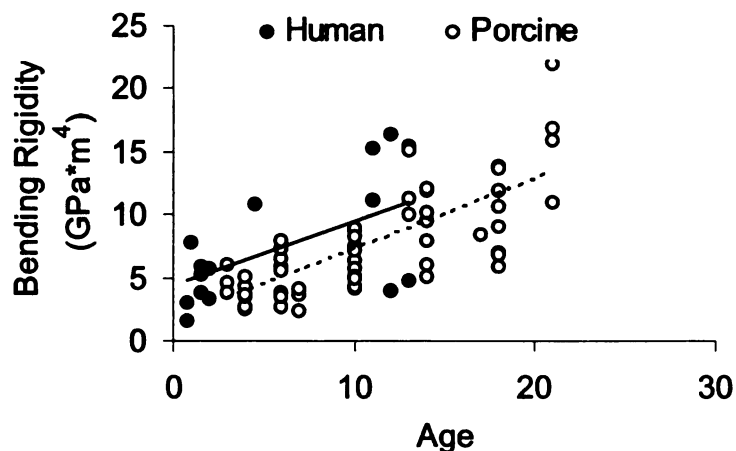


Figure 2.10. Bending rigidity of human and porcine specimens versus age (Human – months; porcine – days). The human data was based on data from Coats and Margulies (2006) and unpublished data from Li et al (2007).

velocity (0.025 m/sec). While a previous study by Wood (1971) shows that the bending modulus of adult human cranial specimens between twenty-five and ninety-five years of age increases with increases in strain rate, the previous study by Coats and Margulies (2006) showed no strain rate dependency in bending modulus with age for specimens less than one month of age. Future studies may be needed to more fully examine rate dependencies in both the human and porcine infant cranial bone during early developmental ages.

The current study was also performed to document potential changes in the mechanical properties of the infant porcine coronal suture as a function of age. Margulies and Thibault (2000) show a significant difference between the bone-suture-bone and bone specimen mechanical properties for two to three day old porcine specimens. The data from the current study was in agreement with this finding up to fourteen days. Specifically, in the current study, the bone-suture-bone specimens were less stiff, absorbed more energy to failure, and withstood larger bending deformation before failure than the bone specimens. The differences between bone-suture-bone specimens and bone specimens changed significantly in the current study between fourteen and eighteen days. During this period of development, the bone-suture-bone specimens underwent a significant increase in stiffness, a significant decrease in the energy absorbed to failure, and a decrease in strain at failure. These changes resulted in mechanical properties of the bone-suture-bone specimens that were more similar to those of the bone specimens at eighteen and twenty-one days. The explanation for this change between fourteen and eighteen days is currently unclear from visual analysis of the specimen cross-sections. This could also be related to changes in the biochemical make-

up of the suture itself during this period. Some gross changes in the morphology of the porcine bone did appear to occur over the time period of the current study. One important feature was the development of two distinct layers of bone. Examination of each cross-section revealed isolated pockets of porous bone beneath an outer, more compact layer of bone in specimens as young as three days. By fourteen days, a clear separation between the compact and porous layers could be seen over the entire cross-section of these specimens. Previous studies on human (McElhaney et al., 1970; Behrens et al., 1974) and bovine (Martin, 1984) samples have shown that small increases in porosity of bone specimens can result in large decreases in their ultimate stress. The Coats and Margulies (2006) study also documents an increase in ultimate stress with specimen age, but our analysis of postnatal data alone out to thirteen months again revealed no statistical change with age. These observations warrant additional studies on the morphological development of human and porcine infant parietal bone.

The current study also showed no significant difference in orientation on the bending properties of parietal beam specimens. This finding was in contrast to previously published data for human specimens up to 40 weeks of gestation (McPherson and Kriewall, 1980). Interestingly, the aforementioned study described a distinct fiber orientation in both pre-term and term human infant parietal bones, but visual observation of the developing infant porcine skull did not show any distinct spiculae that might be related to a fiber orientation effect. While this finding seemed to reveal an inconsistency between infant human and porcine skulls, we were not able to find definitive information on when this visible fiber orientation effect disappears in humans.

In summary, the current investigation documented alterations in the mechanical properties of beam specimens from the porcine infant skull with age. While it remains difficult to correlate these changes with those that may occur in the human pediatric patient, due to limited human pediatric data, the current study has attempted to make a correlation by combining existing and new, unpublished data. A good correlation appeared to exist for days of pig age and months of human age in terms of flexural rigidity of the beam specimens. Such a correlation may lend support to the notion that studies on the developing porcine model may provide an important biomechanical tool for the study of pediatric skull fracture in efforts to investigate cases of childhood abuse.

REFERENCES

- Behrens J, Walker P, and Shoji H., 1974, "Variations in Strength and Structure of Cancellous Bone at the Knee," *Journal of Biomechanics*, **7**, pp. 201-7.
- Belfer R, Klein B, and Orr L., 2001, "Use of the Skeletal Survey in the Evaluation of Child Maltreatment," *American Journal of Emergency Medicine*, **19**, pp. 122-4.
- Bertocci G. and Pierce M., 2006, "Applications of Biomechanics Aiding in the Diagnosis of Child Abuse," *Clinical Pediatric Emergency Medicine*, **7**, pp. 194-9.
- Coats B. and Margulies S., 2006, "Material Properties of Human Infant Skull and Suture at High Rates," *Journal of Neurotrauma*, **23(8)**, pp. 1222-32.
- Dickerson J. and Dobbing J., 1966, "Some Peculiarities of Cerebellar Growth in Pigs," *Proceedings of the Royal Society of Medicine*, **59**, pp. 1088.
- Herring S. and Teng S., 2000, "Strain in the Braincase and Its Sutures During Function," *American Journal of Physical Anthropology*, **112**, pp. 575-93.
- Holck P., 2005, "What Can a Baby's Skull Withstand? Testing the Skull's Resistance on an Anatomical Preparation," *Forensic Science International*, **151**, pp. 187-91.
- Kemp A, Dunstan F, Harrison S, Morris S, Mann M, Rolfe K, Datta S, Thomas D, Sibert J, and Maguire S., 2008, "Patterns of Skeletal Fractures in Child Abuse: Systematic Review," *B.M.J.*, **337**, pp. 1-8.
- Li H, Ruan J, Xie Z, Wang H, and Liu W., 2007, "Investigation of the Critical Geometric Characteristics of Living Human Skulls Utilising Medical Image Analysis Techniques," *Int. J. Vehicle Safety*, **2(4)**, pp. 345-61.
- Margulies S. and Thibault K., 2000, "Infant Skull and Suture Properties: Measurements and Implications for Mechanisms of Pediatric Brain Injury," *Journal of Biomechanical Engineering*, **122**, pp. 364-71.
- Martin R., 1984, "Porosity and Specific Surface of Bone," *Critical Reviews in Biomedical Engineering*, **10**, pp. 179-222.
- McElhaney J, Fogle J, Melvin J, Haynes R, Roberts V, and Alem N., 1970, "Mechanical Properties of Cranial Bone," *Journal of Biomechanics*, **3**, pp. 495-511.
- McPherson G. and Kriewall T., 1980, "The Elastic Modulus of Fetal Cranial Bone: A First Step Towards an Understanding of the Biomechanics of Fetal Head Molding," *Journal of Biomechanics*, **13**, pp. 9-16.

Mertz H., 1984, "A Procedure for Normalizing Impact Response Data," SAE #840884, 29th Stapp Car Crash Conference, Chicago, IL.

Meservy C, Towbin R, McLaurin R, Myers P, and Ball W., 1987, "Radiographic Characteristics of Skull Fractures Resulting From Child Abuse," A.J.R., **149**, pp. 173-5.

Pierce M, Valdevit A, Anderson L, Inoue N, and Hauser D., 2000, "Biomechanical Evaluation of Dual-Energy X-Ray Absorptiometry for Predicting Fracture Loads of the Infant Femur for Injury Investigation: An In Vitro Porcine Model," Journal of Orthopaedic Trauma, **14(8)**, pp. 571-6.

Reece R. and Sege R., 2000, "Childhood Head Injuries: Accidental or Inflicted," Archives of Pediatric Adolescent Medicine, **154**, pp. 11-15.

Wood J., 1971, "Dynamic Response of Human Cranial Bone," Journal of Biomechanics, **4**, pp. 1-12.

CHAPTER THREE

AGE-DEPENDENT FRACTURE CHARACTERISTICS OF RIGID AND COMPLIANT SURFACE IMPACTS ON THE INFANT SKULL – A PORCINE MODEL

ABSTRACT

Head injuries account for 80% of fatal child abuse in younger children. However, non-fatal injury from short falls (less than 3 feet) can still result in skull fracture especially for infants less than 12 months of age. In many cases the ability to determine child abuse from accidental injury may be difficult. This study documents skull fracture on infant porcine specimens with respect to age and interface in an effort to identify fracture characteristics for a developing skull under known conditions. A single impact causing fracture was conducted on the skull of porcine specimens aged 2 to 28 days (n=76). Impacts were conducted using a gravity-accelerated mass to deliver a controlled energy impact to the parietal bone. Paired rigid and compliant impacts at the same energy were conducted at each specimen age. Impact force, impact duration, and fracture length were recorded. Pressure sensitive film was used to record contact areas and pressures for each impact. Fracture length was measured to the nearest millimeter. Impact force increased with age for both rigid and compliant interfaces. Contact area for compliant interface impacts increased with age but no change with age was noted for rigid interface impacts. Bone fractures initiated at bone-suture interfaces and not at the point of impact. Diastatic fractures were observed on skulls as early as 4 days of age after impacts with a compliant interface, while rigid interface impacts did not show suture damage until 10 days of age. Diastatic fractures were common for both interfaces on skulls aged 10 to 17 days, but disappeared after 17 days of age. For a given energy, impact of the skull with a

compliant interface caused more fracture damage than with a rigid interface for specimens less than 17 days of age, but less damage for specimens aged 24 to 28 days. The age-dependent response of the developing skull to impact with rigid and compliant surfaces is important in forensic cases for determining potential differences between testimony describing the events leading to injury and the observed fracture pattern.

INTRODUCTION

Head injuries account for 80% of fatal child abuse in younger children (Case et al., 2001), while short falls rarely, if ever, cause serious injury or death (Reiber, 1993). In one study of 89 children under 2 years of age, 19 of the 20 fatalities were due to abuse (Hobb, 1984), while a study of 1,881 falls from bed height reported no deaths (Belechri et al., 2002). However, non-fatal injury from short falls (less than 3 feet) can still result in skull fracture especially for infants less than 12 months of age (Gruskin and Schutzman, 1999). Due to the paucity of skull fracture tolerance data for infants and young children, pediatric trauma involving single-event head injuries with related cranial fractures represent one of the greatest challenges to forensic pathologists and anthropologists.

Distinguishing between abuse and accidental trauma can be difficult, as both may produce similar types of injuries (Billmire and Myers, 1985). Specifically, linear, complex, and depressed fractures can be seen in both types of cases (Reece and Sege, 2000; Wheeler and Shope, 1997). The most commonly fractured cranial bone in both accidental injury and abuse cases is the parietal (Hobb, 1984; Meservy et al., 1987; Leventhal et al., 1993). The risk of injury is also dependent on the contacting surface and fall height (Bertocci et al., 2003; Chalmers et al., 1996). Other variables, such as the area struck, thickness of the skull, thickness of scalp and hair, and impact direction can also affect the fracture pattern (Knight, 1991; Cooperman and Merten, 2001). To develop reliable models for skull fracture prediction, the effects of these aforementioned variables must be better understood.

While several studies have documented important information regarding the response of the infant skull and brain to blunt force impact, these data are limited to one or two age groups. And because of ethical considerations, experimentation on human pediatric specimens is very limited. While scaling of the adult skull has met with some success in predicting impact response of the pediatric skull (Prange et al., 2004), the head of an infant is smaller and geometrically unlike that of an adult (Schneider et al., 1986) and the validity of predicting skull fracture patterns in infants from adult data has not been investigated. Using adult data to predict skull fracture patterns in the pediatric skull may also be problematic due to the different structural (ease of deformation and decreased threshold to fracture) and mechanical properties of the infant skull (Thibault and Margulies, 1998; Prange et al., 2000; Prange and Margulies, 2002). However, one animal model of the human infant has begun to emerge regularly in the current literature. A study by Dickerson and Dobbing (Dickerson and Dobbing, 1967) shows a similarity in development of the central nervous system when correlating months of the human to weeks of the pig. Other studies have used porcine models to predict fracture loads for the infant human femur (Pierce et al., 2000) and strain in the braincase and sutures (Herring and Teng, 2000). More recently, age-related rates of change in the bending rigidity of the infant human and infant porcine skulls has been found to be similar for a correlation based on months in humans to days in pigs (Baumer et al., in press).

The hypotheses of the current study were two-fold. First, impact energy required to initiate a skull fracture would depend on specimen age. Second, the extent of fracture damage for a given energy impact would depend on impact interface. These data using a developing porcine model may provide a baseline for the characterization of fracture

patterns resulting from blunt force impacts onto different contact interfaces for the developing human pediatric skull. These data may have ultimate utility in the study of potential child abuse cases.

MATERIALS AND METHODS

Porcine specimens aged from 2 to 28 days (n=76) were obtained from a local supplier and stored at -20°C . All animals died of natural causes. The specimens were frozen within 12 hours of death. None of the specimens had outward signs of head injury, which was later confirmed during specimen preparation.

Each specimen was thawed at room temperature for 24 hours prior to testing. All soft tissue was removed from the left side of the skull, leaving the periosteum to help prevent drying of the bones and sutures. This side of each skull was placed in a bed of air-hardening epoxy (Fibre Strand, Martin Senour Corp., Cleveland, OH). Capturing the skull in this manner allowed deformation of the skull bones and sutures, but eliminated gross motions (translations and rotations) of the skull as a whole. After the potting material had hardened, the skull was bathed in phosphate-buffered saline (PBS) solution in regular intervals until the experimental impact. Each skull, with the scalp in place, was impacted in the center of the right parietal bone. The impact location was controlled by a custom-made, 4 degree-of-freedom, lockable fixture that was built to hold the potted skull (Figure 3.1). The skull was oriented so that the impact was normal to the bone surface.

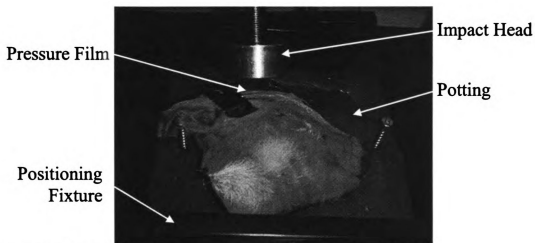


Figure 3.1. Skull positioning and set-up showing rigid impact head.

Each specimen was subjected to a single impact with a gravity-accelerated mass (GAM) (Figure 3.2). A load transducer (4.45 kN capacity, model AL311CV, Sensotec, Columbus, OH) was mounted on the GAM behind the impact interface to record forces. A single impact was assured by using an operational amplifier comparator circuit to monitor the impact forces and energize an electromagnetic solenoid to catch the impactor immediately after the load returned to zero. Two interchangeable impact interfaces were created for the GAM to represent rigid and compliant impact interfaces. The rigid interface was a solid aluminum cylinder with approximately 16 cm² of impact surface. The compliant interface was a deformable aluminum material (1.10 MPa crush strength Hexcel, Hexcel Corp., Stamford, CT), approximately 3 cm thick with a 16 cm² impact surface, fastened to the rigid interface. Both interfaces had greater surface area than the resulting contact area on the skull.

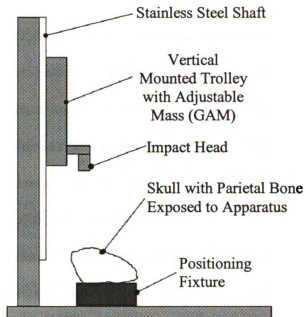


Figure 3.2. Drop test fixture set-up.

Input energy was adjusted by changing the drop height of the 1.67 kg GAM. A second mass of 1.92 kg was necessary for specimens twenty-one days and older, as the drop height was limited in the laboratory. The mass of the impact interface for each impact was included in the total mass of the GAM, and the force data was checked for inertial effects. Preliminary data collected at several ages was used to estimate the input energy needed to initiate a fracture using the rigid interface for each specimen age. In a few cases ($n=7$), the first impact with a rigid interface did not cause a fracture, so a second, higher energy impact was performed. Impacts were always conducted in pairs. All skulls impacted with the compliant interface were impacted at the same energy that caused fracture in the paired rigid impact on another skull of the same age. While the input energy was the same for rigid and compliant impacts at each age, the energy of impact required to cause fracture initiation had to be increased with specimen age. The forces and impact durations were recorded at 10,000 Hz.

Pressure sensitive film packets (Prescale, Fuji Film Ltd., Tokyo, Japan) were attached with tape to the skull at the impact site to measure contact area and pressures generated during impact. Low (0-10 MPa) and medium (10-50 MPa) range pressure films were stacked together and sealed between two sheets of polyethylene (0.04 mm thick) to prevent exposure to fluids during the impact (Atkinson et al, 1998). Using the previously documented procedure, the film was scanned and converted to pressure using a dynamically calibrated density-to-pressure scale. Only the low pressure film was analyzed in these experiments as the pressures were not high enough to record on the medium pressure film.

Computed tomography (CT) scans were conducted for each skull after impact (625 μ m-thick coronal slices). The width of the skull vault and average thickness of the parietal bone were obtained from these scans using reconstruction software (Osirix version 3.0, Open Source General Public License). The width of the vault was measured at its widest point from parietal bone to parietal bone. Average parietal bone thickness was determined from a slice near the center of the parietal bone.

Visual inspection was conducted on each skull after the soft tissue and periosteum were removed from the impacted side. All suture damage and any visible bone fractures were recorded. Each specimen was then cleaned via standard anthropological procedures, removing all remaining soft tissue. Complete fracture diagrams and measurements were made for each specimen. Total length of the skull fractures was measured to the nearest millimeter with a flexible measuring tape, which conformed to the curvature of the skull.

The impact and pressure data were analyzed for age effects using linear regression analyses. Comparisons between the interfaces were performed using a two-factor (age, interface) ANOVA. Statistically significant effects were reported for $p < 0.05$.

RESULTS

Linear regression analyses showed a significant increase (0.0516 mm/day) in average parietal bone thickness with age ($p < 0.001$), but no change in skull vault width with age.

The input energy required to cause fracture increased from 1.5 J at two days of age to 11.5 J at twenty-eight days of age. A characteristic rapid drop in force appeared in the force-time plot for all rigid interface impacts that were associated with fracture (Figure 3). In rigid interface impacts that did not cause fracture, a more pronounced peak was observed. Rapid drops in force during compliant interface impacts could not always be associated with fractures due to the deformation of the interface.

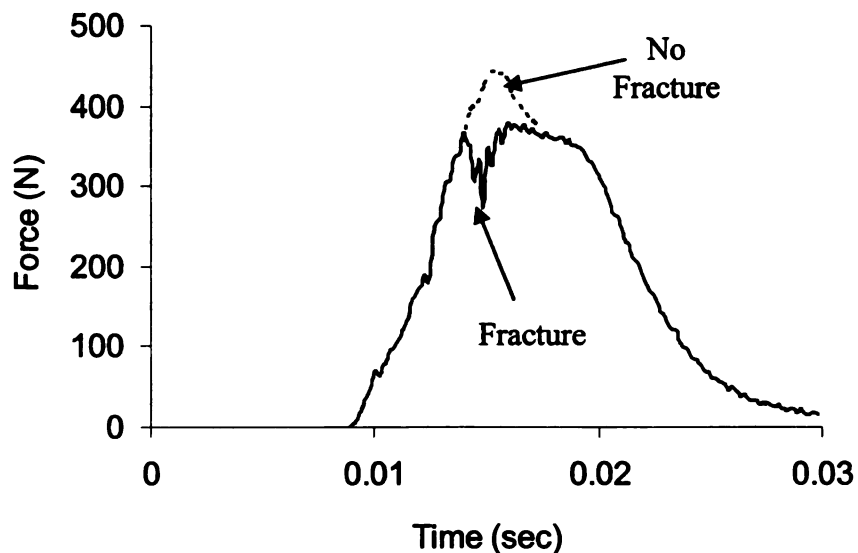


Figure 3.3. Overlay of force-time plots showing typical characteristics of an impact that caused fracture and one that did not.

For both impact interfaces, linear regression analyses showed a significant increase in impact force with age that was required to produce a fracture ($p < 0.001$) (Figure 3.4). The slopes and intercepts of impact forces versus age were not different based on interface.

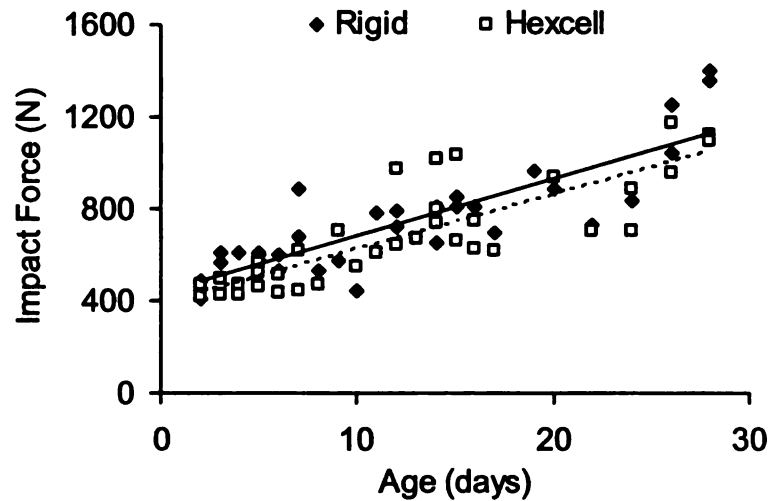


Figure 3.4. Peak force during impact for rigid and compliant interfaces.

The area of contact for the compliant interface significantly increased with age ($p < 0.001$), but no significant change was noted for the rigid interface (Figure 3.5).

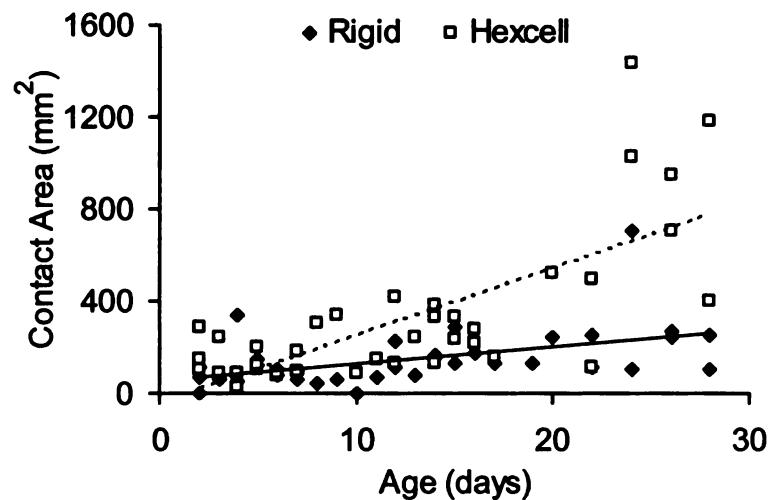


Figure 3.5. Contact area recorded on pressure sensitive film during impacts for rigid and compliant interfaces.

Bone fractures for all ages, and for both interfaces, occurred at sites away from the point of impact (Figure 3.6). These bone fractures initiated at a suture-bone interface. Frequently, bone fractures were accompanied by diastatic fractures that were generally located near the fracture tip at the bone-suture interface. Diastatic fractures caused by a rigid interface impact were not present until specimens were ten days of age, while diastatic fractures caused by a compliant interface were present as early as four days of age (Figure 3.7). Diastatic fractures were common for both interfaces between ten and seventeen days. Neither interface showed suture damage after seventeen days.

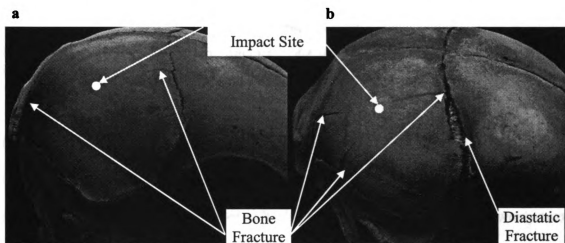


Figure 3.6. Representative fracture sites for (a) rigid and (b) compliant interface impacts (five-day-old specimens shown). Fracture sites initiated at bone-suture boundaries. Compliant interface impact showed increased fracture lengths at similar initiation sites as the rigid interface impacts as well as diastatic fracture of coronal suture.

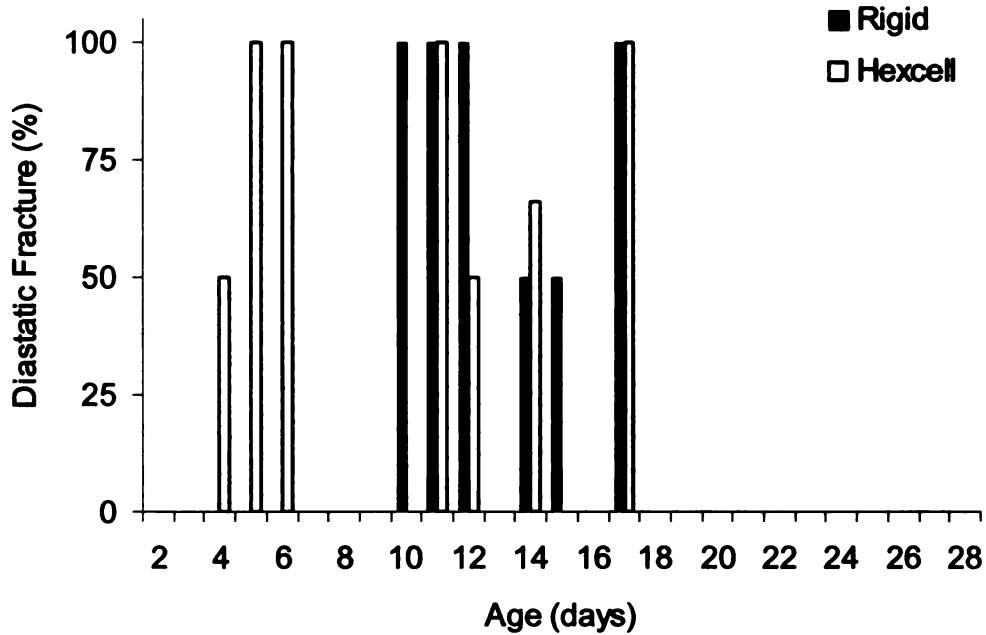


Figure 3.7. Frequency of diastatic fractures caused by both rigid and compliant interfaces versus age.

A two-factor (age, interface) ANOVA performed on the total fracture length (bone and diastatic combined) revealed significantly more damage caused by the compliant interface than by the rigid interface on pig skulls less than seventeen days of age, similar amounts of damage from both interfaces between seventeen and twenty-two days of age, and significantly more damage caused by the rigid interface than by the compliant interface for specimens aged twenty-four to twenty-eight days ($p < 0.05$) (Figure 3.8).

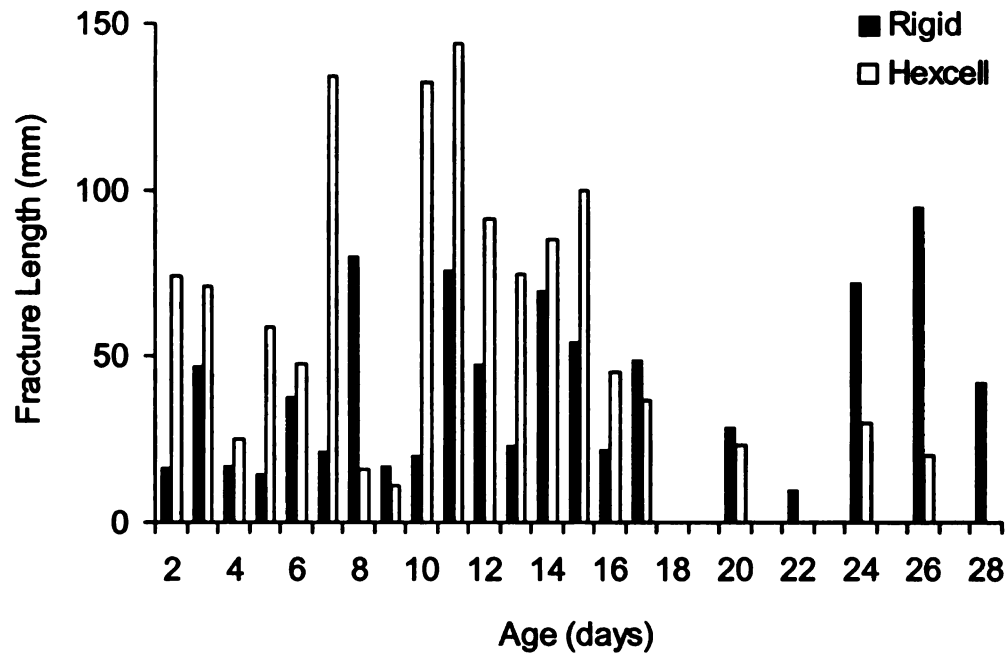


Figure 3.8. (Average) Fracture length generated by rigid and compliant impacts at the same impact energy.

DISCUSSION

In an effort to better understand fracture of the developing skull under known conditions, the current study examined characteristics of impact induced fracture to the infant porcine skull with respect to age and impact interface. As would be expected, the peak impact force increased with age. While an increase in the bending modulus of the porcine skull with age would account for this increase in force with age, a previous study shows that the bending modulus of infant porcine bone and bone-suture-bone specimens under 4-point bending does not change significantly with specimen age (Baumer et al., in press). Measurements of the average parietal bone thickness, however, showed a significant increase with age, which seemed to correlate with changes in the impact force. It is expected that the increasing strength of the skull with age is due to changes in geometry (thickness), and not due to an increase in bone quality with age.

There has been debate in the forensic community as to the mechanism of fracture initiation on adult human skulls. Specifically, whether fractures initiate at the point of impact (Kroman, 2004) or at remote sites of “outbending” (Gurdjian et al., 1950). In the current study, 70 of 76 infant porcine specimens displayed fracture initiation at a suture-bone boundary, and not at the center of the parietal bone (the impact location). The other six specimens involved comminuted skull fractures that obscured the site of initiation. The locations of fracture initiation on infant porcine specimens in the current study agreed with the findings of Gurdjian et al. (1950) for adult human skulls, however it is currently unclear if the fracture initiation sites observed in this study are due to the immature nature of the cranial bone, differences in porcine cranial geometry or a combination these factors. Despite potential differences limiting direct comparisons with adult human fracture information, the infant porcine model developed in the current study showed that fracture initiation occurred in relatively predictable locations at bone-suture interfaces for impacts on the parietal bone against a flat surface. This information may be expanded in the future to other interface conditions and should be correlated with fracture patterns in the human infant skull from case files. These findings suggest that skull fractures on the developing skull from impacts with rigid or compliant flat surfaces may be located remote from the site of the impacting force and nearer to the cranial sutures.

The current study produced a greater amount of fracture on younger infant porcine skulls using a compliant than rigid interface. The concentrated force of an impact with a rigid interface was expected to produce a larger amount of bone fracture than an impact with a compliant interface where the same force intensity would be

distributed over a larger contact area and contact stresses would be reduced. This study, however, showed that the relative amount of fracture between these interfaces was dependent on age. For infant pigs less than seventeen days of age, a compliant interface caused significantly more damage than a rigid interface for the same impact energy, while for specimens twenty-four days of age and older the rigid interface generated more damage than the compliant interface. Specimens younger than seventeen days of age also showed frequent damage to the sutures, while specimens older than seventeen days of age had bone fractures alone. In a previous study on beam specimens cut from infant porcine skulls and loaded in 4-point bending, it has been shown that there is a significant difference in the relationship between bone and bone-suture-bone material properties for specimens aged fourteen and eighteen days (Baumer et al., in press). These changes resulted in a significant increase in the relative strength of the coronal suture at eighteen days to values more similar to that of bone. This effect correlates well with the disappearance of suture damage and a change in interface-dependent fracture differences documented in the current study. The age-dependent response of the developing skull to impact with rigid and compliant surfaces is important in forensic cases for determining potential differences between testimony describing the events leading to injury and the observed fracture pattern. Specifically, the infant porcine model suggests that very young skulls may actually be more susceptible to extensive skull fracturing from an impact against a compliant surface than from an impact against a more rigid surface. Further investigations will be needed to create a more comprehensive set of patterns for various impact interfaces and energies.

In an effort to explain the interface- and age-dependent results of the current study, it was noted that the contact area for the compliant interface impacts was generally greater than that for the rigid interface impacts. Yet, the generated impact force was not different between interfaces. It was hypothesized that the increased contact area for the compliant interface impacts resulted in a higher state of stress close to the boundaries of the parietal bone (sutures). It may then be suspected that the mechanical properties of the sutures were more critical during impacts with a compliant than with a rigid interface. For specimens under seventeen days of age, when the sutures are significantly more compliant than bone, large deformations at the sutures during impact for both interfaces may have generated high levels of stress near the boundaries of the parietal bone at the sutures. Therefore the risk of damage at the suture may have increased, resulting in the high frequency of diastatic fractures. Furthermore, the higher state of peripheral stresses caused by the compliant interface may have promoted fracture propagation, resulting in the increased fracture length documented for the compliant interface versus the rigid interface. The increase in suture strength that occurs between fourteen and eighteen days of age may have allowed a better distribution of impact stresses across the boundaries of the parietal bone, resulting in lower overall levels of stress in the parietal bone and across suture lines. This effect may help explain why in the relatively older infants the compliant interface actually generated less fracturing to the skull than for the rigid interface, since the rigid interface would be expected to generate more localized contact stresses nearer the site of impact.

In summary, this study documented an increase in impact energy required to initiate skull fractures as specimen age increased. Furthermore, there was relatively more

fracture damage generated for a compliant than a rigid interface with equal input energy at the younger infant ages. While a direct correlation with infant human fracture patterns is not currently available from case files, the experimental observations from the developing porcine model may aid in understanding some of the limited data that is available today. The experimental documentation of fracture initiation energy and the extent of skull fracture with respect to interface as a function of specimen age may be of critical importance in future investigations of potential childhood abuse.

REFERENCES

Baumer T, Passalacqua N, Powell B, Fenton T, Haut R., Accepted for Publication, "Age Dependent Mechanical Properties of the Infant Porcine Parietal Bone and a Correlation to the Human," *Journal of Biomechanical Engineering*, in press.

Belechri M, Petridou E, Trichopoulos D., 2002, "Bunk versus conventional beds: a comparative assessment of fall injury risk," *Journal of Epidemiology and Community Health*, **56**, pp. 413-7.

Bertocci G, Pierce M, Deemer E, Aguel F, Janosky J, Vogeley E., 2003, "Using Test Dummy Experiments to Investigate Pediatric Injury Risk in Simulated Short-Distance Falls," *Archives of Pediatric Adolescent Medicine*, **157(5)**, pp. 480-6.

Billmire M. and Myers P., 1985, "Serious head injury in infants: accident or abuse?," *The American Academy of Pediatrics*, **75**, pp. 340-2.

Case M, Graham M, Handy T, Jentzen J, Monteleone J., 2001, "Position Paper on Fatal Abusive Head Injuries in Infants and Young Children," *The American Journal of Forensic Medicine and Pathology*, **22**, pp. 112-22.

Chalmers D, Marshall S, Langley J, Evans M, Brunton C, Kelly A, et al., 1996, "Height and surfacing as risk factors for injury in falls from playground equipment: a case-control study," *Injury Prevention*, **2**, pp. 98-104

Cooperman D. and Merten D., 2001, "Skeletal Manifestation of Child Abuse," In: *Child Abuse: Medical Diagnosis and Management*. Philadelphia: Lippincott, Williams, and Wilkins, pp. 123-56.

Dickerson J. and Dobbing J., 1967, "Prenatal and postnatal growth and development of the central nervous system of the pig," *Proceedings of the Royal Society of London*, **166(1005)**, pp. 384-95.

Gruskin K. and Schutzman S., 1999, "Head Trauma in Children Younger Than 2 Years," *Archives of Pediatric Adolescent Medicine*, **153**, pp.15-21.

Gurdjian E, Webster J, Lissner H., 1950, "The Mechanism of Skull Fracture," *Radiology*, **54(3)**, pp. 313-39.

Herring S. and Teng S., 2000, "Strain in the Braincase and Its Sutures During Function," *American Journal of Physical Anthropology*, **112**, pp. 575-93.

Hobb C., 1984, "Skull Fracture and the Diagnosis of Abuse," *Archives of Disease in Childhood*, **59**, pp. 246-52.

Knicht B., 1991, "Fatal child abuse," In: *Forensic Pathology*. London: Edward Arnold, pp. 457-73.

Kroman A., 2004, "Experimental Study of Fracture Propagation in the Human Skull: A Re-Testing of Popular Theories," *Proceedings of the American Academy of Forensic Sciences*, Dallas, TX, H79:314.

Leventhal J, Thomas S, Rosenfield N, Markowitz R., 1993, "Fractures in young children: distinguishing child abuse from unintentional injuries," *American Journal of Diseases of Children*, **147**, pp. 87-92.

Meservy C, Towbin R, McLaurin R, Myers P, Ball W., 1987, "Radiographic characteristics of skull fractures resulting from child abuse," *American Journal of Roentgenology*, **149**, pp. 173-5.

Pierce M, Valdevit A, Anderson L, Inoue N, and Hauser D., 2000, "Biomechanical Evaluation of Dual-Energy X-Ray Absorptiometry for Predicting Fracture Loads of the Infant Femur for Injury Investigation: An In Vitro Porcine Model," *Journal of Orthopaedic Trauma*, **14(8)**, pp. 571-6.

Prange M, Luck J, Dibb A, Van Ee C, Nightingale R, Myers B., 2004, "Mechanical Properties and Anthropometry of the Human Infant Head," *Stapp Car Crash Journal*, **48**, pp. 279-99.

Prange M. and Margulies S., 2002, "Regional, Directional, and Age-Dependant Properties of the Brain Undergoing Large Deformations," *Journal of Biomechanical Engineering*, **124(2)**, pp. 244-52.

Prange M, Meaney D, Margulies S., 2000, "Defining brain mechanical properties: Effects of region, direction, and species," *Stapp Car Crash Journal*, **44**, pp. 205-13.

Reece R and Sege R., 2000, "Childhood Head Injuries: Accidental or Inflicted," *Archives of Pediatric Adolescent Medicine*, **154**, pp. 11-15.

Reiber G., 1993, "Fatal falls in childhood: How Far Must Children Fall to Sustain Fatal Head Injury?," *American Journal of Forensic Medicine and Pathology*, **14**, pp. 201-7.

Schneider L, Lehman R, Pflug M, Owings C., 1986, "Size and Shape of the Head and Neck From Birth to Four Years," Washington, D.C. The Consumer Product Safety Commission, Report No.: UMTRI-86-2.

Thibault K. and Margulies S., 1998, "Age-Dependant Material Properties of the Porcine Cerebrum: Effect on Pediatric Head Injury Criteria," *Journal of Biomechanics*, **31(12)**, pp. 1119-26.

Wheeler D. and Shope T., 1997, "Depressed skull fracture in a 7-month old who fell from bed," Pediatrics, 100, pp. 1033-4.

CHAPTER FOUR

CHARACTERISTICS AND PREDICTION OF CRANIAL CRUSH INJURIES IN CHILDREN

ABSTRACT

Experimentally applied bilateral crushing forces on adult cadaver skulls and even a few case reports on children have shown similarities in basilar fracture locations. It has even been suggested that the overall path of fracture may be related to the location of applied force on the skull. This study documents 4 clinical cases of fatal crush injuries to young children between 1.5 and 6 years of age with correlations between modeled stress and clinically observed fracture patterns. The damage in the clinical cases was concentrated in the basicranium. Each of the cases presented fracture patterns that bridged the impact sites and traversed the middle cranial fossa in the area of the spheno-occipital synchondrosis. The crushing forces observed in the clinical cases were recreated on a simplified finite element model of a cranium by applying bilateral pressures to regions correlating to the specific exterior injury locations of each case. Numerous trials were run within the elastic range of bone to develop a representative and clearly characterized pattern of principal stress directions. Areas of tensile stress were assumed to be the most likely location(s) of potential fracture. The regions of largest tensile stress developed on the skull were compared to the clinically observed fracture patterns in the 4 cases, revealing that locations of high tensile stress in all four cases were located on the basicranium with low levels of stress on the cranial vault. Additionally, regions of high tensile stress appeared to follow the fracture path(s) extending from the location of maximum stress. These results suggest that pre-failure stress field diagrams may give

some insight into the projected fracture propagation paths, although prediction will not be exact. Also, these analyses of the modeled stresses and the clinically observed fractures suggest that quasi-static bilateral loading of the cranium may lead to predictable fracture of the basicranium, possibly independent of age.

INTRODUCTION

Fracture interpretation is a necessary component of forensic analysis and contributes to the determination of the cause and manner of death. Skeletonized remains, in particular, lack skin and scalp abnormalities that enhance the complete description of a head injury or injuries. Thus, a clear understanding of fracture propagation becomes vital to the forensic professional. Head injuries are often the result of dynamic forces in which a moving object strikes the cranium at a considerable speed or the cranium makes contact with a static object that causes it to rapidly decelerate (Duhaime et al., 1995). In cases of crushing injuries, however, a static load is applied relatively slowly to the cranium, initially causing deformation with eventual fracturing if pressure continues or increases. In experimental tests on the effects of bilateral crushing forces on cadaver skulls, Russell and Schiller (1949) report that avulsion of the petrous portion, fracture through the dorsum sellae, and principal fracture lines running in the direction of the compressive forces were common features observed.

There are several case reports of basilar skull damage in the literature involving both crushing and impulse based loading scenarios mainly focusing on adult crania. A study of 15 cases of crushing injuries to adult skulls aged 14-63 years and experimentally induced crushing fractures on 11 cadaver crania revealed similarities in basilar fracture patterns (Russell and Schiller, 1949). However, a study by Harvey and Jones (1979) claimed that fractures through both petrous bones was not an indicator of impact site. Another study by Yasue (1981) then suggested that the overall path of fracture through the basicranium could, in fact, be related to the region of the skull impacted. More recently, a study by Kroman (2005) attempted to produce cranial base

(hinge) fractures in two unembalmed cadaver adult human crania specimens using a drop tower. High-speed video demonstrated that fractures initiated at the site of impact and propagated through the middle cranial fossa, with some additional minor fractures surrounding the foramen magnum. In this study the vaults had been removed so it is unclear if the fractures would have terminated at the points of applied forces (fixture and impactor). Kroman further notes a very wide separation of the failing bones during impact which no doubt would cause very severe soft-tissue damage in the cranial base; this correlates to the high amount of energy and lethality involved in these scenarios.

It is assumed that fractures will generally follow the path of least resistance, but this path may be different between the child and adult cranium. While all of the aforementioned studies focused on adult crania, some recent case reports on quasi-static loading to the crania of children have also presented observations of basilar fractures (Takeshi et al., 2005; Duhaime et al., 1995). The trend of quasi-static loading producing basilar fractures in both adults and children may suggest that prediction of these fractures is possible.

The Finite Element (FE) method is a powerful analytical modeling tool that can be used to determine internal stresses and strains within a complex solid. Several studies have shown that maximum principal stress (or strain) directions from a modeled structure correlate well with areas of experimentally or clinically observed bone fractures (Graham et al., 2000; Silva et al., 1998; Doorly and Gilchrist, 2006). While modeling of fracture propagation generally involves high computational costs, one theory suggests that there is a close, although not exact, relationship between pre-failure stress trajectories and the ultimate path of propagation. In brief, Frank and Lawn (1967)

proposed that crack growth occurs in such a way as to maximize the energy dissipation per unit length of growth, and that the greatest amount of dissipation occurs when the crack plane is perpendicular to the direction of greatest principal tensile stress. In other words, the directions of principal tensile stress developed on a solid may be a reasonable predictor of propagation direction.

In this study, four cases of childhood fatalities from crushing head injuries inflicted by vehicle tires exhibited similar fracture patterns despite differences in age and extent of force. This raised the question as to whether certain fracture patterns are indicative of bilateral crushing injuries and if these could be predicted based on the type of loading and the biomechanical properties of the skull.

MATERIALS AND METHODS

Four clinical cases of fatal crush injuries to young children between 1.5 and 6 years of age under known conditions were used as a baseline for applied forces and resulting fracture patterns. In all cases the skull was trapped between a vehicle tire and the ground. The contact sites and skull fractures were identified and diagramed during autopsy by the investigating forensic pathologist (M.N.). Biomechanical modeling was then conducted in an attempt to recreate and explain the similarities exhibited in the fracture patterns of these cases.

A simplified model of a skull was created in a finite element package (Abaqus v.6.3, Hibbitt, Karlsson & Sorensen, Inc., Pawtucket, RI, USA) (Figure 4.1). This model consisted of symmetry about the sagittal plane, but not about the coronal or transverse planes. Each major bone of the vault was modeled separately, assumed to have a uniform thickness, and constrained at the suture joints to form the full cranial model.

The base of the cranium was modeled as a flat surface with the same thickness as the vault. The primary landmarks in the basal region were modeled: a hole was added to simulate the foramen magnum, dense oblong extrusions lateral to the foramen magnum were generated to represent the petrous portions, and anterior to the foramen magnum the thickness was reduced to represent the region of the sphenoid-occipital synchondrosis.

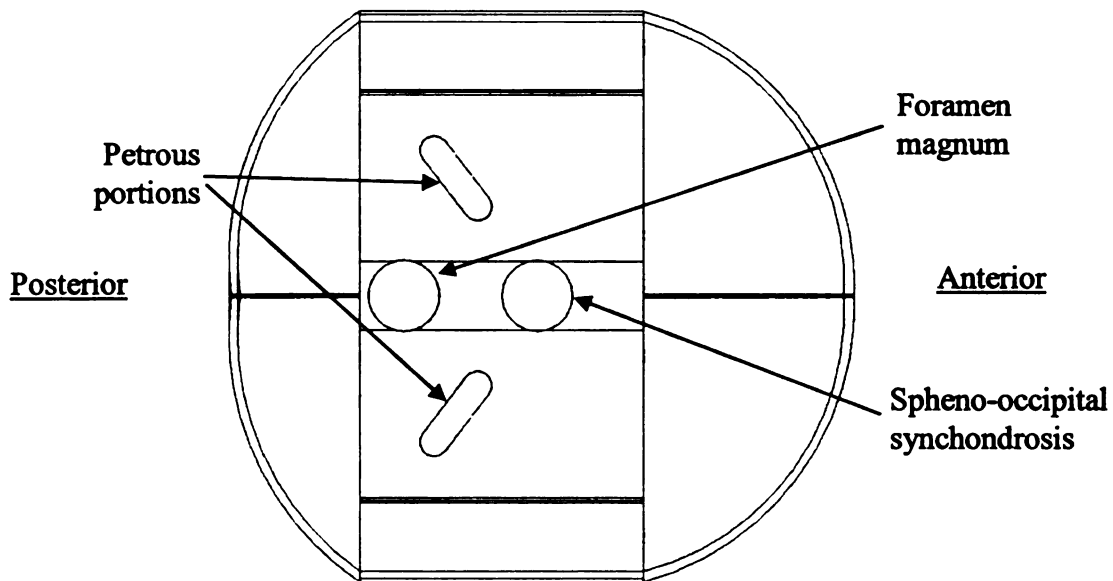


Figure 4.1. Simplified cranial model showing modeled landmarks of the basicranium. View of endocranial surface with vault removed.

FE analysis was utilized in an effort to reproduce and examine possible relationships between the theoretical pre-failure stresses developed on the skull and the fracture patterns observed clinically. The magnitude of the force applied to the cranial model was the same in every case and was scaled down such that the modeled cranium would not actually fail. The crushing forces reported in the clinical cases were recreated by applying the force over a region of the cranium correlating to the specific exterior injury locations for each case. Numerous trials were run within the elastic range of bone to develop a representative and clearly characterized pattern of principal stress and strain

directions. Areas of tensile (principal) stress were assumed to be the most likely location(s) of potential fracture.

RESULTS

CASE REPORTS

Case 1

A 5-year-old female child was struck by her family's sedan when she fell in an attempt to stop the vehicle after her brother accidentally engaged the transmission. Her head was run over by the right front tire of the car. The autopsy revealed an intact cranial vault with a cranial base fracture that traversed the lateral right anterior cranial fossa, the midline of the middle cranial fossa, and the left lateral aspect of the posterior cranial fossa. This fracture bridged the blunt impact sites on the right anterior and left posterior aspects of the head.

Case 2

An unhelmeted 6-year-old male was struck by a car while riding his bike. His head was run over by the vehicle's left rear tire. Autopsy revealed an intact cranial vault. The cranial base, however, was bisected by a gaping X-shaped fracture centered in the midline of the middle cranial fossa. There were two adjacent arms of the fracture in the right middle cranial fossa. The other two adjacent arms were in the posterior aspect of the left middle cranial fossa and the anterior aspect of the left posterior cranial fossa. This fracture bridged the blunt impact sites on the right anterior and lateral aspects of the head and the left lateral and posterolateral aspects of the head.

Case 3

A 3-year-old male was run over attempting to run away from a farm grain wagon that had begun to roll. His head was run over by one of the wheels of the wagon. Autopsy revealed gaping linear fractures that traversed the parietal bones and the right

and left sides of the frontal bone. One end of each fracture intersected the widely gaping right side of the coronal suture, other ends were continuous with fractures of the cranial base. A dominant cranial base fracture traversed the left petrous bone, the midline of the middle cranial fossa, the anterior aspect of the right middle cranial fossa and the posterolateral aspect of the right anterior cranial fossa. Additional intersecting fractures were centered in the left middle and posterior cranial fossae.

Case 4

A 1.5-year-old female was entrapped under a small moving van and her head was run over by the right rear wheel. Autopsy revealed an intact cranial vault but extensive intersecting fractures of the cranial base that predominately traversed the middle and posterior cranial fossae from side to side. A large fracture also bisected the anterior cranial fossae.

Fracture Pattern Similarities

Each of the cases presented fracture patterns that bridge the impact sites and traversed the middle cranial fossa in the area of the spheno-occipital synchondrosis. Additionally, the damage was concentrated in the basicranium leaving the cranial vault intact in all cases except the 3-year-old boy impacted by the farm grain wagon. Furthermore, general amounts of fracture increased with inferred increase in magnitude of applied force (grain-wagon vs. car) or decrease in age.

The four cases presented three contact scenarios with four different fracture patterns. Specifically, the contact forces in Case 1 were applied primarily to the frontal and occipital bones in a direction between anterior-posterior and lateral (Figure 4.2a), the contact forces in Cases 2 and 3 were also applied to the frontal and occipital bones

but had an additional lateral component (Figure 4.2b, c), and the contact forces in Case 4 were applied to the lateral surfaces of the cranial model (Figure 4.2d).

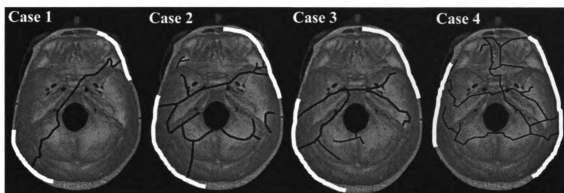


Figure 4.2. Diagrams of fractures due to quasi-static crushing forces to skulls aged (a) 5 years – Case 1, (b) 6 years – Case 2, (c) 3 years – Case 3, and (d) 1.5 years – Case 4. White cranial margins represent contact of applied forces (ground and tire).

FE Analysis

Modeling of all four cases revealed that locations of high tensile stress and high tensile strain were located on the basicranium. There were some areas of lower tensile stress at the sites of the applied load and in a few areas on the cranial vault, but due to the assumption that failure would occur at locations of high stress, these areas were ignored for this analysis. The maximum tensile stress for all models were similar (standard deviation of $\pm 5\%$). The tensile stresses developed on the skull were filtered to display only the highest 20% for correlation to fracture patterns. The length of the arrow at each location represented the relative magnitude of stress at that location.

Case 1 presented the simplest fracture pattern as a single linear fracture traversing the basicranium from the right greater wing of the sphenoid across the spheno-occipital synchondrosis to the left lateral portion of the occipital, connecting the loading sites (Figure 4.3a). An overlay of the directions of maximum principal tensile stresses revealed a linear concentration on the right side of sphenoid and in the area of

the speno-occipital synchondrosis, which correlated well with sections of the observed fracture (Figure 4.3b).

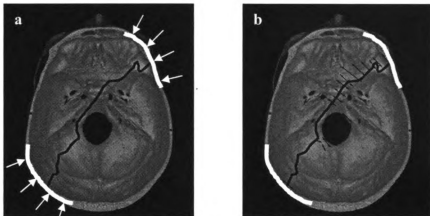


Figure 4.3. (Case 1) Crushing injury to the skull of a 5-year-old. Diagrams of (a) clinically observed fractures and (b) an overlay of the highest 20% of principal tensile stresses produced from a FE model. White cranial margins represent contact of applied forces (ground and tire).

Cases 2 and 3 presented slightly more complex fracture patterns. In part, the complexity was increased due to the similarities in loading but dissimilarities in fracture (Figure 4.4a and Figure 4.5a, respectively). A similar fracture in both cases stretched from the right aspect of the sphenoid through the sella turcica and along the superior aspect of the petrous portion of the temporal. The overlay of the directions of maximum principal tensile stresses was identical in both cases due to the similarity of loading patterns. There was correlation between the stress and the fracture for both cases, especially along the line of similar fracture, although each had areas of high stress where fracture did not occur (Figure 4.4b and Figure 4.5b).

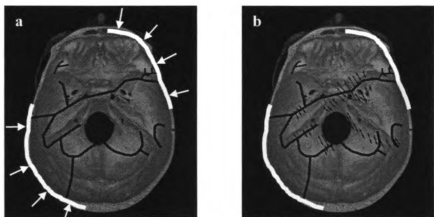


Figure 4.4. (Case 2) Crushing injury to the skull of a 6-year-old. Diagrams of (a) clinically observed fractures and (b) an overlay of the highest 20% of principal tensile stresses produced from a FE model. White cranial margins represent contact of applied forces (ground and tire).

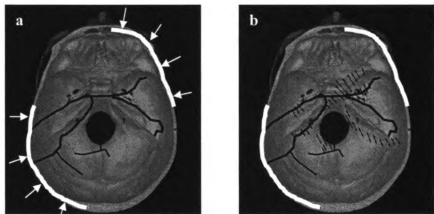


Figure 4.5. (Case 3) Crushing injury to the skull of a 3-year-old. Diagrams of (a) clinically observed fractures and (b) an overlay of the highest 20% of principal tensile stresses produced from a FE model. White cranial margins represent contact of applied forces (ground and tire).

Case 4 presented the most complex fracture pattern extending both longitudinally and transversely through the basicranium (Figure 4.6a). Fractures ran longitudinally across the midline of the anterior cranial fossa, and horizontally through the middle and posterior cranial fossa with various areas of comminution. The overlay of the directions of maximum principal tensile stresses revealed an area of complex stress in the same area as the highly comminuted fracture of the right side of the cranial base. Additionally,

a more linear pattern of stresses occurred near the fractures on the left side of the skull (Figure 4.6b).

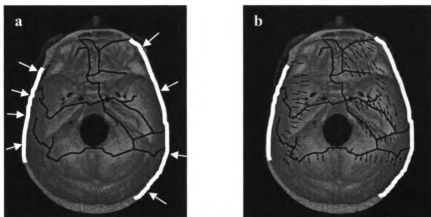


Figure 4.6. (Case 4) Crushing injury to the skull of a 1.5 year old. Diagrams of (a) clinically observed fractures and (b) an overlay of the highest 20% of principal tensile stresses produced from a FE model. White cranial margins represent contact of applied forces (ground and tire).

DISCUSSION

The analyses performed in this study represent a quantitative, theoretical attempt to correlate stress and strain intensities and their distributions to fracture patterns on the skull caused by quasi-static bilateral pressures. A linear, small strain, isotropic, uniform thickness model of a human calvarium was constructed to maintain some manageability in the preliminary modeling. Analyses of the modeled stresses and the clinically observed fractures suggested that quasi-static bilateral loading of the cranium may lead to predictable fracture of the basicranium, although the predictions were not exact. The promising nature of these results suggest that it may be useful to develop a more complex model for a more accurate prediction of fractures on a case-by-case basis.

The location of maximum tensile stress would be expected to be the site of fracture initiation, and the location of maximum stress in each of the four models correlated well with the area(s) of fracture in each of the clinical cases. However, Frank

and Lawn (1967) also suggest that paths of high tensile stress may approximate the path of fracture propagation. In the four cases presented in this study, regions of high tensile stress appeared to follow the path of the fracture extending from the location of maximum stress. Fracture propagation, however, requires increasing levels of stress to overcome the dissipation of energy that occurs with the previous fracturing. These increasing levels of stress may ultimately result in additional fracture sites on the material surface (Paterson and Wong, 2005). Two or more isolated regions of the skull developed high tensile stresses in Cases 2-4, which may have resulted in multiple sites of fracture initiation with propagation extending from each site. Multiple initiation sites with subsequent propagation joining the sites could explain the complexity of the fractures seen in Cases 2-4, as opposed to the singular region of fracture and stress intensity developed in Case 1. The four cases presented in this study suggest that pre-failure stress field diagrams may, in fact, give some insight into the projected fracture propagation paths and, ultimately, fracture patterns developed during quasi-static bilateral loading of the cranium.

The cases and analyses presented in this study supported some general trends for quasi-static bilateral loading scenarios. Autopsy revealed fractures through the middle cranial fossa in the region of the spheno-occipital synchondrosis in all cases. Modeling displayed high tensile stresses through this region in Cases 1-3; with Cases 2 and 3 developing maximum levels of stress at this landmark. However, modeling of Case 4 showed no region of high tensile stress passing through the spheno-occipital synchondrosis. Interestingly, Case 4 involved the youngest child and one of the most massive vehicles (moving van). This result may suggest that the material model should

be altered as a function of age, especially for the very young pediatric patient. Autopsies also revealed fractures connecting the loading sites through the basicranium in all four cases. The models showed regions of high tensile stress in this region for Cases 1-3, although the tensile stresses in Case 4 did not seem to follow the same pattern. Intact cranial vaults were also present in three of four cases. The models displayed no significant levels of stress on the vault that would be expected to cause fracture. It is possible that the mass of the vehicle (grain wagon) caused excessive fracture propagation that was not able to be modeled in Case 3. All of the fracture related observations seen in the current study showed similarities to experimentally developed fractures on adult cadaver skulls (Russell and Schiller, 1949) suggesting that these patterns of quasi-static loading of the cranium may be somewhat age independent, except for the very young patient; likely as a function of cranial geometry which would remain essentially the same throughout life.

In summary, a simple model of a cranium subjected to clinically observed bilateral crushing forces was largely able to predict the characteristics of the developed fracture patterns. The results of this study were not meant to propose that the theoretical stresses developed on this simplified cranial model actually predict an arbitrary fracture pattern developed clinically. These results do show that a simplified analysis of tensile stresses developed from some basic information on boundary loads and locations on the cranium can generate patterns of fracture that are consistent with clinical fractures. The four cases in conjunction with the FE model suggest that craniums subjected to bilateral crushing forces tend to fracture in predictable ways. Further, the regions of high tensile

stress that develop between the locations of loading on the pediatric cranium coincide with the locations of tensile fracture.

The predictability of this pediatric cranial fracture pattern has practical application. Medical examiner and coroner death investigations attempt to establish circumstances of injury. In cases of unknown or questionable circumstances, this fracture pattern would suggest a particular mechanism of injury (relatively slow application of a static load) consistent with a heavy wheeled vehicle. The described fracture pattern would be less consistent with other, more common injuries such as those sustained in motor vehicle collisions (ejection or internal tumbling) and in the setting of inflicted blunt trauma. This information may prove relevant in clarifying unexplained perimortem events in cases of crushing injuries to the pediatric cranium, particularly if information from examination of skin and scalp is not possible due to skeletonization.

REFERENCES

- Doorly M, Gilchrist M., 2006, "The use of accident reconstruction for the analysis of traumatic brain injury due to head impacts arising from falls," *Computer Methods in Biomechanics and Biomedical Engineering*, **9(6)**, pp. 371-7.
- Duhaime A-C, Eppley M, Margulies S, Heher K, Bartlett S., 1995, "Crush Injuries to the Head in Children," *Neurosurgery*, **37(3)**, pp. 401-7.
- Frank F, Lawn B., 1967, "On the Theory of Hertzian Fracture," *Proceedings of the Royal Society of London*, **299(1458)**, pp. 291-306.
- Graham R, Oberlander E, Stewart J, Griffiths D., 2000, "Validation and use of a finite element model of C-2 for determination of stress and fracture patterns of anterior odontoid loads," *Journal of Neurosurgery (Spine 1)*, **93**, pp. 117-25.
- Harvey F, Jones A., 1980, "'Typical' Basal Skull Fracture of Both Petrous Bones: An Unreliable Indicator of Head Impact Site," *Journal of Forensic Sciences*, **25(2)**, pp. 280-6.
- Paterson M, Wong T., 2005, "Griffith Theory of Brittle Failure," In: *Experimental Rock Deformation – The Brittle Field*. Berlin: Springer, pp. 45-57.
- Russell W, Schiller F., 1949, "Crushing Injuries to the Skull: Clinical and Experimental Observations," *Journal of Neurology, Neurosurgery, and Psychiatry*, **12**, pp. 52-60.
- Silva M, Keaveny T, Hayes W., 1998, "Computed Tomography-Based Finite Element Analysis Predicts Failure Loads and Fracture Patterns for Vertebral Sections," *Journal of Orthopaedic Research*, **16**, pp. 300-8.
- Takeshi M, Okuchi K, Nishiguchi T, Seki T, Watanabe T, Ito S, et al., 2006, "Clinical Analysis of Seven Patients of Crushing Head Injury," *The Journal of Trauma-Injury, Infection, and Critical Care*, **60(6)**, pp. 1245-9.
- Tortosa J, Martinez-Lage J, Poza M., 2004, "Bitemporal Head Crush Injuries: Clinical and Radiological Features of a Distinctive Type of Head Injury," *Journal of Neurosurgery*, **100**, pp. 645-51.
- Yasue M., 1981, "Clinical and experimental investigation of mediobasal skull fracture," *Neurol Med Chir (Tokyo)*, **21**, pp. 1041-9.

CHAPTER FIVE

FINITE ELEMENT MODELING OF RIGID AND COMPLIANT SURFACE IMPACTS TO THE PEDIATRIC PORCINE PARIETAL BONE

ABSTRACT

Head injuries account for 80% of fatal child abuse in younger children. Yet, in many cases the ability to determine child abuse from accidental injury may be difficult. Head injuries may occur when a moving object strikes the cranium at a considerable speed or when the cranium strikes a static object that causes the skull to rapidly decelerate. This study documents theoretical principal stress and strain directions developed on a cranial model with respect to age and interface in an effort to identify fracture characteristics for the developing skull under known conditions. The impact conditions generated experimentally for rigid and compliant interface impacts to porcine skulls of various ages were recreated on a simplified finite element model. The model accounted for changes in bone thickness as well as material properties of bone and suture with age. Numerous trials were run within the elastic range of the materials to develop a representative and clearly characterized pattern of pre-failure principal stress and strain directions. Maximum principal stress and strain directions revealed distinct locations of expected fracture regardless of age or interface. However, the extent and magnitude of strains at any given location were dependent on both age and interface. Experimental results showed that blunt force trauma to the parietal bone consistently resulted in fracture at the bone-suture boundaries of the parietal bone, which correlated well with areas of high strain. Young specimens showed high levels of strain in the sutures while old specimens showed limited frequency and magnitude of strain within the sutures.

These findings correlated well with previous findings of significantly higher rates of suture failure in young specimens than in old specimens. However, suture damage only occurred experimentally in 29% of younger specimens, while bone fracture occurred in 97%. Due to the relative differences in the elastic moduli of bone and suture it was expected that similar levels of strain could cause failure of the bone prior to failure of the sutures. Interestingly, the larger contact area generated during compliant interface impacts also seemed to produce strains within the bone distributed nearer the parietal bone boundaries. This distribution of high strains may have promoted propagation of fractures initiating at the boundaries, resulting in the greater amount of observed damage on the cranium produced from compliant interface impacts.

INTRODUCTION

Skull fracture interpretation is a necessary component of forensic analysis and contributes to the determination of the manner and cause of death. Head injuries are often the result of dynamic forces in which a moving object strikes the cranium at a considerable speed or the cranium makes contact with a static object that causes the skull to rapidly decelerate (Duhaime et al., 1995). Head injuries account for 80% of fatal child abuse in younger children (Case et al., 2001). Yet similar types of injuries can be generated by abusive and accidental trauma (Billmire and Myers, 1985) and, due to the paucity of cranial fracture tolerance data for infants and young children, pediatric trauma involving single-event head injuries with related cranial fractures represent one of the greatest challenges to forensic pathologists and anthropologists. Thus, a clear understanding of fracture patterns becomes vital to the forensic professional.

While several studies have documented important information regarding the response of the infant cranium and brain to blunt force impact, these data are limited to one or two age groups. And because of ethical considerations, experimentation on human pediatric specimens is very limited. Scaling of the adult cranium has met with some success in predicting impact response of the pediatric cranium (Prange et al., 2004) but, the head of an infant is smaller and geometrically unlike that of an adult (Schneider et al., 1986) and the validity of predicting cranial fracture patterns in infants from adult data has not been investigated. Using adult data to predict fracture patterns in the pediatric cranium may also be problematic due to the different structural (ease of deformation and decreased threshold to fracture) and mechanical properties of the infant cranium (Thibault and Margulies, 1998; Prange et al., 2000; Prange and Margulies,

2002). However, one animal model of the human infant has begun to emerge regularly in the current literature. A study by Dickerson and Dobbing (1967) shows a similarity in development of the central nervous system when correlating months of the human to weeks of the pig. Other studies have used porcine models to predict fracture loads for the infant human femur (Pierce et al., 2000) and strain in the braincase and sutures (Herring and Teng, 2000). More recently, age-related rates of change in the bending rigidity of the infant human and infant porcine craniums has been found to be similar for a correlation based on months in humans to days in pigs (Baumer et al., in press).

The Finite Element (FE) method is a powerful analytical modeling tool that can be used to determine internal stresses and strains within a complex solid. Several studies have shown that maximum principal stress (or strain) directions from a modeled structure correlate well with areas of experimentally or clinically observed bone fractures (Graham et al., 2000; Silva et al., 1998; Doorly and Gilchrist, 2006). While modeling of fracture propagation generally involves high computational costs, one theory suggests that there is a close, although not exact, relationship between pre-failure stress/strain trajectories and the ultimate path of propagation. In brief, Frank and Lawn (1967) propose that crack growth occurs in such a way as to maximize the energy dissipation per unit length of growth, and that the greatest amount of dissipation occurs when the crack plane is perpendicular to the direction of greatest principal tensile stress. In other words, the directions of principal tensile stress developed on a solid may be a reasonable predictor of the propagation path.

In this study, blunt impact trauma to the center of the parietal bone was modeled for comparison to fracture patterns experimentally generated on the developing porcine

cranium. The hypothesis was that age and interface characteristics of a given impact would define the stress and strain fields developed on the cranium, leading to predictable fracture patterns. A secondary goal was to examine possible stress or strain related causes for the experimentally generated fractures that consistently occurred away from the impact site at the bone-suture boundaries (Chapter 3).

MATERIALS AND METHODS

A simplified model of a porcine cranium was created in a finite element package (Abaqus v.6.3, Hibbitt, Karlsson & Sorensen, Inc., Pawtucket, RI, USA) using dimensions from CT scans of impacted crania. Most elements of the cranial geometry were accounted for, although some regions were simplified due to the distance from the area of interest and complexity of meshing (Figure 5.1). The curvature of the parietal bone was determined from CT scans and a 5-point spline was used to simulate the measured curvature. The average bone thickness of the parietal bone was taken from specimens tested in 4-point bending and was altered with age, but the modeled bone was assumed to have a uniform thickness. The sutures were given a more pronounced width than observed on the actual cranium since the material properties used in the model were not directly obtained from sutures, but involved the bone on both sides of the sutures as well. The primary landmarks in the basal region were included, but the specific undulations were removed and replaced by a flat plate with the same thickness as the rest of the cranium. A region of the frontal bones was modeled, but the snout and orbits were removed. The model consisted of symmetry about the sagittal plane, but not about the coronal or transverse planes. Each bone and suture of the cranium was modeled separately and constrained at the bone-suture interfaces to form the full cranial model.

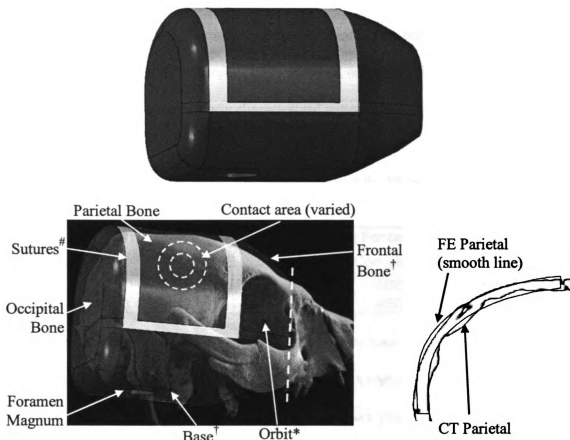


Figure 5.1. Simplified cranial model with overlays of modeled structures on true structures. Coronal cut of CT used for thickness comparison. *Feature not modeled. †Feature simplified. #Suture width altered for consistency with material property data obtained previously. Dotted line represents location of frontal bone removal.

Finite Element (FE) analysis was utilized in an effort to produce and examine the expected stresses and strains developed on the cranium and to compare these stresses and strains to experimentally observed fracture patterns with respect to both age and interface. The thickness of the cranium and the material properties of the bone and suture were altered in the model to represent changes in age. Age related changes in the elastic moduli of bone and suture were taken from experimental results of a previous study (Baumer et al., in press), and average impact force and contact area data from another study were used to simulate the difference between a rigid and a compliant interface

(Chapter 3) (see Table 1). Briefly, the rigid interface was constrained to produce smaller contact areas than the compliant interface with both interfaces producing the same magnitude of impact force. Numerous trials were run within the elastic range of bone to develop a representative and clearly characterized pattern of principal stress and strain directions.

Table 5.1. (Average) properties used in development of the FE model and impact conditions.

Specimen Age	Elastic Modulus		Impact Force		Contact Area	
	E_{sut}	E_{bone}	Rigid	Compliant	Rigid	Compliant
Young (3-7 days)	3.38	7.21	561	508	94	119
Old (18-21 days)	3.37	5.29	930	860	176	322

The magnitude of principal stress and strain directions were filtered to remove the lowest 20%. The remaining stresses and strains were compared to the experimentally produced fracture patterns. A representative cranium from young and old specimens impacted by each interface was selected. Each chosen cranium displayed all the common fracture sites from the age/interface and no instances of uncommon sites. A photo editing program (Photoshop ..) was used to overlay the modeled stresses and strains onto a photograph of the chosen, experimentally fractured cranium.

RESULTS

An overlay of maximum principal tensile stress directions revealed a concentration at the impact site for all age-interface combinations (Figure 5.2). The length of the arrow at each location represents the relative magnitude of stress at that location. Comparison of these overlays revealed distinct lines of expected fracture between suture boundaries and the impact point, regardless of age or interface. However, the proximity of the stress field to the boundary varied by interface. Specifically, larger

regions of high tensile stresses were located nearer the suture-bone boundary for compliant interface impacts than for rigid interface impacts. Furthermore, tensile stresses developed in the sutures of the young specimens were significantly greater for compliant interface impacts than for rigid interface impacts. The old specimens had similar levels of stress in the sutures for both interfaces.

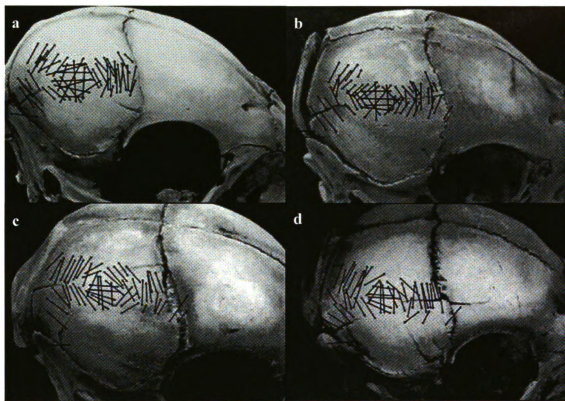


Figure 5.2. Overlay of maximum principal tensile stresses from FE models on representative experimental cranial fractures for (a) rigid interface impact to a young specimen, (b) rigid interface impact to an old specimen, (c) compliant interface impact to a young specimen, and (d) compliant interface impact to an old specimen. Longer lines represent higher stresses.

An overlay of the directions of maximum principal tensile strain revealed high strains at or near bone-suture boundaries, with lower levels of strain at the impact site for all age-interface combinations (Figure 5.3). The rigid interface impacts produced higher levels of strain closer to the impact site than the compliant interface impacts, however, the highest strains were still located away from the impact site. Furthermore, the

magnitude of the tensile strains developed in the sutures of the young specimens from compliant interface impacts was considerably greater than those from rigid interface impacts. The old specimens had similar levels of strain in the sutures for both interfaces. Comparison of these overlays revealed some possible paths of expected fracture between bone-suture boundaries and the impact point.

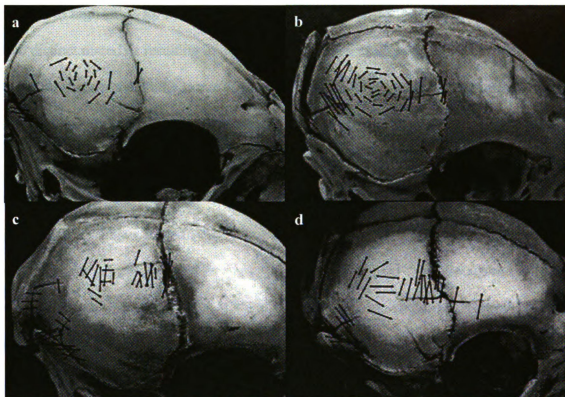


Figure 5.3. Overlay of maximum principal tensile strains from FE models on representative experimental cranial fractures for (a) rigid interface impact to a young specimen, (b) rigid interface impact to an old specimen, (c) compliant interface impact to a young specimen, and (d) compliant interface impact to an old specimen. Longer lines represent higher strains.

DISCUSSION

Modeling of a cranium with sutures resulted in a heterogeneous structure and, therefore, regions of high stress did not necessarily correspond to regions of high strain. Specifically, high stresses were generally located near the point of impact in the center of the parietal bone, while high strains were located at or near bone-suture boundaries.

Experimental results showed that blunt force trauma to the parietal bone consistently resulted in fracture at the bone-suture boundaries of the parietal bone (Chapter 3), which correlated well with areas of high strain. The correlation of fracture to strain has been previously documented in a study on failure of vertebral sections by Silva et al., (1998). The study suggests that regions of high strain may be a better predictor of failure than regions of high stress for heterogeneous structures. However, the current study utilizes two distinct materials resulting in different failure criteria for each. It has been shown that strains generated in the suture of the developing porcine skull during normal function can be 6 times greater than the strain developed in the bone (Herring and Teng, 2007) and in 4-point bending failure tests the strain in the suture can be 2 to 3 times greater than the strain in bone (Baumer et al., in press). Thus, it would be expected that initial material failure would occur in bone prior to suture for conditions of similar strain. Therefore, the strains in the bone near the boundaries of the parietal bone, which were slightly lower than the strains developed in the sutures, likely resulted in failure prior to failure of the suture structure in most cases.

Age effects played an important role in the distribution of strains on the cranium. The young specimens showed more frequent and greater magnitudes of strain in the sutures than the old specimens, which correlated well with the experimentally observed patterns of suture failure (Chapter 3). Specifically, the developing skull from birth to sixteen days of age showed significantly higher rates of suture failure than specimens over sixteen days of age. The old specimens showed much higher frequency and magnitude of strain within the bone than the young specimens with some lower magnitude strains in the sutures. This shifting of strain from the sutures to the bone with

increasing age was likely related to the changes in suture properties observed between fourteen and eighteen days of age (Baumer et al., in press). Overall, the modeled patterns of strain seemed to support the general characteristics of experimentally generated fracture with regard to age.

The compliant interface produced high strains within and near the sutures while the rigid interface produced more localized strains around the impact site with lower magnitudes of strain in the sutures. The larger contact area during compliant interface impacts seemed to result in strains distributed nearer the parietal bone boundaries. This difference in the proximity of strain in the bone to the bone-suture boundaries may help explain the greater extent of fracture in compliant interface impacts at young ages. Specifically, higher levels of strain near the boundaries may have promoted propagation of fractures initiating at the boundaries, resulting in greater damage to the skull from compliant interface impacts.

Despite the difference in proximity to the parietal bone boundaries, both interfaces produced higher levels of strain away from the point of impact than at the point of impact. At young ages, both interfaces produced high strains that were largely constrained to the coronal and temporal sutures. However, suture damage was only seen in 29% of specimens aged under 16 days, while bone fracture occurred in 97% of these specimens (Chapter 3). This suggests that the sutures were better able to absorb the high strains while the slightly lower levels of strain observed in the parietal bone resulted in material failure. Of course, some suture damage was generated experimentally, suggesting that the sutures were not always able to fully absorb the high strains. It is currently unclear if the sutures in these cases failed before or after the bone, but it may

be reasonable to assume, based on the modeled strains, that the suture damage occurred after bone failure. The large strains developed in the suture model with relatively low frequency of experimental damage may suggest that prediction of suture failure on a case-by-case basis may be difficult. However, the correlation between a reduction in magnitude of strain and the disappearance of damage in the sutures for older skulls suggests that some element of predictability may exist.

In summary, a simple model of a porcine cranium subjected to the effects of experimentally induced blunt force trauma to the parietal bone was largely able to predict characteristics of observed fracture patterns. The maximum principal strain directions generated from the model seemed to correlate well with locations of fractures seen in a previous study (Chapter 3). The results of this study were not meant to propose that the theoretical stresses or strains developed on this simplified cranial model actually predict an arbitrary fracture pattern developed experimentally. The results do show that a simplified analysis of tensile strains and, to some extent, stresses developed from some basic information on material properties of the cranium and interface specific loading patterns can generate patterns that are consistent with some aspects of experimental fractures. The experimentally obtained fractures in conjunction with the FE model suggest that blunt impact trauma to the parietal bone of the developing cranium leads to predictable fracture locations. This information may prove relevant in determining perimortem events in forensic cases of head injuries to the pediatric patient with unknown or questionable circumstances.

REFERENCES

Baumer T, Passalacqua N, Powell B, Fenton T, Haut R., Accepted for Publication, "Age Dependent Mechanical Properties of the Infant Porcine Parietal Bone and a Correlation to the Human," *Journal of Biomechanical Engineering*, in press.

Billmire M. and Myers P., 1985, "Serious head injury in infants: accident or abuse?," *The American Academy of Pediatrics*, **75**, pp. 340-2.

Case M, Graham M, Handy T, Jentzen J, Monteleone J., 2001, "Position Paper on Fatal Abusive Head Injuries in Infants and Young Children," *The American Journal of Forensic Medicine and Pathology*, **22**, pp. 112-22.

Dickerson J. and Dobbing J., 1967, "Prenatal and postnatal growth and development of the central nervous system of the pig," *Proceedings of the Royal Society of London*, **166(1005)**, pp. 384-95.

Doorly M, Gilchrist M., 2006, "The use of accident reconstruction for the analysis of traumatic brain injury due to head impacts arising from falls," *Computer Methods in Biomechanics and Biomedical Engineering*, **9(6)**, pp. 371-7.

Duhaime A-C, Eppley M, Margulies S, Heher K, Bartlett S., 1995, "Crush Injuries to the Head in Children," *Neurosurgery*, **37(3)**, pp. 401-7.

Frank F, Lawn B., 1967, "On the Theory of Hertzian Fracture," *Proceedings of the Royal Society of London*, **299(1458)**, pp. 291-306.

Graham R, Oberlander E, Stewart J, Griffiths D., 2000, "Validation and use of a finite element model of C-2 for determination of stress and fracture patterns of anterior odontoid loads," *Journal of Neurosurgery (Spine 1)*, **93**, pp. 117-25.

Herring S. and Teng S., 2000, "Strain in the Braincase and Its Sutures During Function," *American Journal of Physical Anthropology*, **112**, pp. 575-93.

Pierce M, Valdevit A, Anderson L, Inoue N, and Hauser D., 2000, "Biomechanical Evaluation of Dual-Energy X-Ray Absorptiometry for Predicting Fracture Loads of the Infant Femur for Injury Investigation: An In Vitro Porcine Model," *Journal of Orthopaedic Trauma*, **14(8)**, pp. 571-6.

Prange M, Luck J, Dibb A, Van Ee C, Nightingale R, Myers B., 2004, "Mechanical Properties and Anthropometry of the Human Infant Head," *Stapp Car Crash Journal*, **48**, pp. 279-99.

Prange M, Meaney D, Margulies S., 2000, "Defining brain mechanical properties: Effects of region, direction, and species," *Stapp Car Crash Journal*, **44**, pp. 205-13.

Prange M. and Margulies S., 2002, "Regional, Directional, and Age-Dependant Properties of the Brain Undergoing Large Deformations," *Journal of Biomechanical Engineering*, **124(2)**, pp. 244-52.

Schneider L, Lehman R, Pflug M, Owings C., 1986, "Size and Shape of the Head and Neck From Birth to Four Years," Washington, D.C. The Consumer Product Safety Commission, Report No.: UMTRI-86-2.

Silva M, Keaveny T, Hayes W., 1998, "Computed Tomography-Based Finite Element Analysis Predicts Failure Loads and Fracture Patterns for Vertebral Sections," *Journal of Orthopaedic Research*, **16**, pp. 300-8.

Thibault K. and Margulies S., 1998, "Age-Dependant Material Properties of the Porcine Cerebrum: Effect on Pediatric Head Injury Criteria," *Journal of Biomechanics*, **31(12)**, pp. 1119-26.

CHAPTER SIX

CONCLUSIONS AND RECOMMENDATIONS FOR FUTURE WORK

The previous chapters describe the material and fracture characteristics of the developing porcine skull. The bone and suture properties were obtained through 4-point bending experiments on beam specimens removed from the cranium. The parietal bone was impacted under controlled laboratory settings to produce fracture patterns with regard to age and surface interface. A simplified model of the infant cranium was developed in a finite element program for comparison of theoretical stresses and strains with observed fracture patterns. The model was used to simulate clinical cases of bilateral crushing injuries as well as blunt impact trauma to the parietal bone.

In Chapter 2, beam specimens cut from porcine crania were tested in 4-point bending at 25mm/sec until failure to obtain material properties of the bone and suture. While the mechanical properties of parietal bone and coronal suture did not change significantly with age, bone specimens showed an increase in bending stiffness with age. Bone-suture-bone specimens showed an increase in bending stiffness only between 14 and 18 days of age. Correlation analyses using existing and new data to compute the bending rigidity of infant parietal bone specimens suggested that days of pig age may correlate with months of human age during the most common time frame of childhood abuse cases. Future studies should investigate the possible rate sensitivity of the developing bone and suture, specifically focusing on high rate loading to simulate impact rates.

In Chapter 3, skull fracture on infant porcine specimens with respect to age and interface were documented in an effort to identify fracture characteristics for a

developing skull under known conditions. Fractures on the infant porcine skull due to impact with a flat surface initiated at points outside the zone of contact for both rigid and compliant impact interfaces. The skulls of young infants suffered relatively more extensive fracture damage striking a compliant versus a rigid interface for the same impact energy. As the animal aged, however, the damage caused by the compliant interface decreased until no damage was present at energies causing fracture with a rigid impact interface. Future studies should examine additional interfaces of impact, especially involving common surfaces of potential accidental injury such as carpeting or playground rubber. Additionally, the extent of propagation and fracture patterns developed under higher energy impacts should be documented.

In Chapter 4, four clinical cases of fatal crush injuries to young children between 1.5 and 6 years of age were documented with correlations between modeled stress and clinically observed fracture patterns. Regions of high tensile stress in all four cases were located on the basicranium and appeared to follow the fracture path(s) extending from the location of maximum stress. These results suggest that pre-failure stress field diagrams may give some insight into the projected fracture propagation paths, although prediction will not be exact. Also, these analyses of the modeled stresses and the clinically observed fractures suggest that quasi-static bilateral loading of the cranium may lead to predictable fracture of the basicranium, possibly independent of age. Additional case studies would be helpful in validating the model further. Future studies may also be able to obtain more accurate results using CT scans of infant crania. With CT scans, the actual density distribution within the skull could be accounted for rather than the approximation used in this study. Also, the skull dimensions and basal landmark

geometry were approximated. Approximate thickness changes with age were the only geometric property altered.

In Chapter 5, the impact conditions generated experimentally for rigid and compliant interface impacts to porcine skulls of various ages were recreated on a simplified finite element model of a cranium. Experimental results showed that blunt force trauma to the parietal bone consistently resulted in fracture at the bone-suture boundaries of the parietal bone, which correlated well with areas of high strain. The theoretical strains also showed similarities with the significantly higher rates of suture failure in young specimens than in old specimens. Interestingly, the larger contact area generated during compliant interface impacts also seemed to produce strains within the bone distributed nearer the parietal bone boundaries, which may have promoted propagation of fractures accounting for the greater amount of observed damage on the cranium produced from compliant interface impacts. Future studies should develop a model of the skull from exact dimensions of a CT scan.

The information presented in this thesis documents baseline information for fractures generated on the developing porcine skull. An age-based correlation with porcine specimens may provide an important biomechanical tool for the study of pediatric skull fracture in efforts to investigate cases of childhood abuse. This information may prove relevant in clarifying unexplained perimortem events in cases of injuries to the pediatric cranium. Modeling cranial fracture is particularly important in unwitnessed injury cases or in cases where information from examination of skin and scalp is not possible due to skeletonization. These data present several factors that must be examined on a case-by-case basis and may ultimately lead to the deciding factor in a courtroom verdict.

APPENDIX A
RAW DATA FROM CHAPTER 2

Table A.1. Raw data collected from 4-point bending tests of bone-suture-bone specimens.

Specimen	Age	Load (N)	Displacement (mm)	Stiffness (N/m)	Strain Energy (J)	Ult. Stress (MPa)	Ult. Strain (mm/mm)	Bending Modulus (GPa)	Thickness (mm)
PP22	4	14.42	12.09	322.33	0.162	431.83	0.0206		0.91
PP24	3	34.75	13.05	278.56	1.095	1458.14	0.0205	23.49	0.72
PP26	4	12.11	11.26	276.36	0.133	186.85	0.0246	4.06	0.96
PP30	4	13.29	11.37	256.16	0.173	195.82	0.0240	3.42	1.14
PP41	4	19.68	11.81	198.75	0.488	330.17	0.0270	2.89	1.23
PP02	6	29.46	12.94	719.70	0.307	208.12	0.0431	3.19	1.47
PP03	6	13.54	12.12	256.45	0.180	303.43	0.0222	5.01	1.02
PP05	6	12.97	11.38	262.48	0.160	477.70	0.0166	7.41	0.95
PP06	6	17.19	13.13	143.72	0.515	96.50	0.0545	0.95	1.55
PP07	7	26.67	11.94	220.94		224.84	0.0342	2.77	1.19
PP08	7	14.65	13.12	298.43	0.180	187.13	0.0309	4.32	1.14
PP17	6	41.24	13.10	326.69	1.30	457.06	0.0362	4.00	1.28
PP18	6	14.58	12.05	159.63	0.334	104.19	0.0409	1.64	1.35
PP33	6	9.78	11.52	267.77	0.090	180.22	0.0254	4.92	1.15
PP13	10	11.56	10.81	265.35	0.126	104.46	0.0341	3.31	1.31
PP16	10	11.09	12.88	211.79	0.146	70.69	0.0446	1.11	1.64
PP34	14	7.19	4.97	1485.71	0.009	14.68	0.0309	1.36	3.07
PP35	10	28.25	12.59	593.34	0.337	168.62	0.0446	1.47	2.10
PP09	13	24.15	12.71	241.86		151.25	0.0514	1.30	1.80
PP11	14	23.95	10.13	721.30	0.199	106.35	0.0420	2.34	1.96
PP31	14	7.08	8.83	483.94	0.026	42.53	0.0323	2.37	1.75
PP32	14	21.21	9.71	397.15	0.284	126.20	0.0371	2.16	1.72

Table A.1. Continued

Specimen	Age	Load (N)	Displacement (mm)	Stiffness (N/m)	Strain Energy (J)	Ult. Stress (MPa)	Ult. Strain (mm/mm)	Bending Modulus (GPa)	Thickness (mm)
PP19	18	43.95	12.59	247.63	1.957	335.14	0.0401	1.82	1.47
PP20	18	51.67	13.01	498.44	1.343	213.12	0.0561	1.35	2.05
PP21	17	7.64	5.11	1391.43	0.011	36.30	0.0209	3.91	2.12
PP27	18	5.67	4.01	1279.03	0.006	25.08	0.0152	3.08	2.08
PP28	18	5.32	7.08	920.08	0.008	20.90	0.0301	2.58	2.03
PP42	21	5.17	6.77	800.25	0.008	18.88	0.0310	1.94	2.19
PP43	21	4.71	4.99	981.59	0.006	22.95	0.0209	2.81	2.16
PP44	21	3.41	4.94	900.72	0.003	73.38	0.0086	6.69	1.44
PP45	21	4.72	5.85	641.42	0.009	23.87	0.0222	2.59	1.82

Table A.2. Raw data collected from 4-point bending tests of perpendicular bone specimens.

Specimen	Age	Load (N)	Displacement (mm)	Stiffness (N/m)	Strain Energy (J)	Ult. Stress (MPa)	Ult. Strain (mm/mm)	Bending Modulus (GPa)	Thickness (mm)
PP22	4	5.99	9.55	397.86	0.023	400.66	0.0108	5.00	1.30
PP23	4	3.35	8.78	265.78	0.011	356.45	0.0075	5.42	1.07
PP24	3	7.63	9.56	366.76	0.040	565.05	0.0099	7.71	0.83
PP25	3	5.84	6.86	364.13	0.023	247.84	0.0085	12.17	0.87
PP26	4	2.63	9.85	351.92	0.005	80.75	0.0158	8.76	1.00
PP03	6	25.44	12.09	455.30	0.360	708.53	0.0207	15.46	0.84
PP04	6	12.49	10.42	537.21	0.073	567.23	0.0134	14.29	0.95
PP05	6	4.85	8.39	352.23	0.017	177.82	0.0125	5.05	1.16
PP06	6	7.56	7.89	980.44	0.015	62.84	0.0250	7.86	1.47
PP07	7	18.72	11.65	283.88	0.309	897.49	0.0137	3.18	1.20
PP08	7	31.05	12.88	306.65	0.788	465.46	0.0318	4.87	1.20
PP17	6	6.33	11.07	544.32	0.018	218.38	0.0179	8.62	1.21
PP18	6	13.03	4.47	2480.74	0.017	82.29	0.0147	7.84	1.94
PP33	6	21.01	10.58	771.47	0.143	414.83	0.0196	8.62	1.24
PP12	10	7.19	10.73	428.09	0.030	151.95	0.0203	5.45	1.23
PP13	10	14.67	11.43	553.21	0.097	271.97	0.0239	7.59	1.23
PP14	10	6.42	9.30	532.05	0.019	272.62	0.0117	6.48	1.21
PP15	10	13.52	11.36	571.16	0.080	192.75	0.0251	7.21	1.20
PP16	10	15.37	11.00	843.58	0.070	224.33	0.0229	10.87	1.16
PP29	10	13.48	10.18	1111.71	0.041	89.26	0.0335	6.17	1.60
PP35	10	8.29	6.31	1380.32	0.012	99.48	0.0159	4.44	2.00
PP09	13	7.38	8.45	692.52	0.020	148.41	0.0153	5.90	1.36
PP10	13	8.66	8.37	1184.38	0.016	125.74	0.0185	8.09	1.50
PP11	14	15.18	9.44	1426.80		294.99	0.0167	6.25	1.64
PP31	14	9.10	7.04	1381.77	0.015	87.71	0.0188	6.37	1.70
PP32	14	10.85	8.88	1240.05	0.024	122.71	0.0224	5.04	1.79

Table A.2. Continued

Specimen	Age	Load (N)	Displacement (mm)	Stiffness (N/m)	Strain Energy (J)	Ult. Stress (MPa)	Ult. Strain (mm/mm)	Bending Modulus (GPa)	Thickness (mm)
PP32	14	10.85	8.88	1240.05	0.024	122.71	0.0224	5.04	1.79
PP19	18	2.70	3.94	570.59	0.003	68.50	0.0070	6.02	1.38
PP20	18	8.62	3.64		0.007	164.09	0.0069	7.89	2.00
PP21	17	6.37	3.33	1843.82	0.005	110.79	0.0064		1.58
PP27	18	5.92	5.15	1238.42	0.007	76.23	0.0113	6.77	1.56
PP28	18	5.35	8.48	553.22	0.013	124.75	0.0153	3.99	1.51
PP42	21	10.80	3.82		0.009	55.93	0.0136	5.58	2.33
PP43	21	9.68	6.45	1528.13	0.015	54.04	0.0233	4.28	2.05
PP44	21	5.92	5.03	1210.01	0.007	80.26	0.0112		1.30
PP45	21	9.57	4.22	1910.68	0.012	55.70	0.0146	5.35	2.03

Table A.3. Raw data collected from 4-point bending tests of parallel bone specimens.

Specimen	Age	Load (N)	Displacement (mm)	Stiffness (N/m)	Strain Energy (J)	Ult. Stress (MPa)	Ult. Strain (mm/mm)	Bending Modulus (GPa)	Thickness (mm)
PP22	4	5.15	8.89	476.42	0.014	208.14	0.0127	7.16	1.21
PP23	4	4.57	6.35	386.61	0.014	258.37	0.0078	10.36	1.02
PP24	3	6.63	10.40	296.15	0.037	333.24	0.0136	9.23	0.96
PP25	3	2.71	9.63	241.60	0.008	213.73	0.0095	7.53	0.92
PP30	4	6.50	7.14	860.79	0.012	138.76	0.0136	7.33	1.44
PP02	6	10.57	12.35	677.12	0.041	124.82	0.0292	3.60	1.57
PP04	6	14.24	12.12	270.93	0.188		0.0124	9.77	0.90
PP05	6	13.58	13.12	216.92	0.213	414.96	0.0201	4.85	0.99
PP06	6	10.34	9.31	1073.45	0.025	125.65	0.0234	7.42	1.52
PP07	7	7.56	7.89	980.44	0.015	349.43	0.0096		0.91
PP08	7	5.27	8.34	509.36	0.014	82.33	0.0191	5.59	1.34
PP17	6	5.67	7.07	614.77	0.013	121.14	0.0137	10.48	1.16
PP18	6	9.39	13.08	213.56	0.104	457.86	0.0178	4.58	1.08
PP12	10	18.06	13.12	300.47		314.83	0.0292	3.53	1.30
PP13	10	2.47	5.72	326.49	0.005	55.80	0.0110	3.67	1.36
PP14	10	8.78	11.34	374.55	0.052	266.44	0.0188	5.00	1.25
PP15	10	25.49	12.32	439.27			0.0234	7.77	1.13
PP16	10	3.46	7.72	405.91	0.007	121.23	0.0109	4.36	1.29
PP29	10	6.27	4.48	1273.50	0.008	100.16	0.0100	4.29	2.00
PP35	10	33.04	13.11	1196.57	0.229	222.93		7.20	1.72
PP09	13	7.32	9.41	440.47	0.031	175.22	0.0171	5.23	1.29
PP10	13	9.81	9.22	962.99	0.025	239.23	0.0164	7.93	1.45
PP11	14	4.93	5.05	830.08	0.007	63.55	0.0122	4.17	1.71
PP31	14	25.38	12.03	767.03		614.68	0.0240	5.31	1.62
PP32	14	18.63	12.55	598.85			0.0155	3.14	1.59
PP34	14	19.42	8.06		0.036	80.40	0.0356	2.68	2.61

Table A.3. Continued

Specimen	Age	Load (N)	Displacement (mm)	Stiffness (N/m)	Strain Energy (J)	Ult. Stress (MPa)	Ult. Strain (mm/mm)	Bending Modulus (GPa)	Thickness (mm)
PP19	18	2.90	5.07	436.49	0.005	59.20	0.0092	3.90	1.36
PP20	18	8.04	8.20	1192.64	0.014	94.17	0.0216	5.17	1.83
PP21	17	4.55	3.89	1125.39	0.005	68.33	0.0091	4.77	1.87
PP27	18	5.29	5.65	1071.24	0.007	92.82	0.0117	7.82	1.51
PP28	18	3.74	6.96	492.30	0.007	97.66	0.0121	3.32	1.57
PP42	21	7.09	5.45	1185.73	0.011	60.70	0.0170	2.79	2.29
PP43	21	7.76	8.30	845.01	0.018	70.42	0.0251	4.03	1.78
PP44	21	7.32	5.58	1048.29	0.013	106.85	0.0129	9.30	1.43
PP45	21	7.48	4.67	1246.04	0.011	47.05	0.0168	3.68	2.10

Table A.4. Raw data collected from 4-point bending tests of bone-suture-bone specimens NOT resulting in suture failure.

Specimen	Age	Load (N)	Displacement (mm)	Stiffness (N/m)	Strain Energy (J)	Ult. Stress (MPa)	Ult. Strain (mm/mm)	Bending Modulus (GPa)	Thickness (mm)
PP25	3	10.51	11.91	243.53	0.11	888.82	0.011	6.59	0.95
PP26a	4	25.01	12.87	317.92	0.50	1830.07	0.014	6.16	0.94
PP04	6	13.62	10.73	98.20	0.47	616.40	0.013	2.21	0.98
PP33	6	24.81	11.89	239.76	0.64	1020.57	0.017	2.92	1.27
PP09	13	24.15	12.71	241.86	0.604	151.25	0.0514	1.30	1.80
PP10	13	18.49	12.08	274.72	0.312	339.87	0.0263	2.50	
PP12	10	16.19	13.12	290.32	0.23	223.78	0.031	2.22	1.45
PP14	10	14.98	11.67	297.46	0.19	707.72	0.015	2.66	1.39
PP15	10	39.74	12.37	287.36	1.38	830.16	0.025	1.37	1.75
PP29a	10	23.09	11.50	706.36	0.19	152.84	0.038	2.03	1.99
PP29b	10	27.15	12.38	492.38	0.38	553.99	0.024	2.11	1.76
PP44	21	3.41	4.94	900.72	0.00	73.38	0.009	6.69	1.44

Table A.5. Raw data collected from 4-point bending tests for multiple bone-suture-bone specimens taken from the same cranium.

Specimen	Age	Load (N)	Displacement (mm)	Stiffness (N/m)	Strain Energy (J)	Ult. Stress (MPa)	Ult. Strain (mm/mm)	Bending Modulus (GPa)	Thickness (mm)
PP30a	4	6.25	12.14	233.91	0.04	107.67	0.026	3.99	1.14
PP30b	4	13.29	11.37	256.16	0.17	195.82	0.024	3.42	1.15
PP35a	10	28.25	12.59	593.34	0.34	168.62	0.045	1.47	
PP35b	10	6.00	7.06	920.85	0.01	18.96	0.033	2.17	2.11
PP31a	14	7.08	8.83	483.94	0.03	42.53	0.032	2.37	1.75
PP31b	14	67.98	13.11	712.57	1.63	337.11	0.055	2.76	1.90
PP32a	14	21.21	9.71	397.15	0.28	126.20	0.037	2.16	1.72
PP32b	14	60.57	11.71	467.58	1.97	271.66	0.049	1.71	1.87
PP34a	14	7.19	4.97	1485.71	0.01	14.68	0.031	1.36	
PP34b	14	11.90	6.72	1395.30	0.03	27.73	0.038	0.93	3.32
PP27a	18	5.67	4.01	1279.03	0.01	25.08	0.015	3.08	2.08
PP27b	18	5.67	3.89	1762.55	0.00	44.58	0.011	5.05	1.94
PP28a	18	7.80	4.29	1739.99	0.01	33.43	0.016	4.81	1.93
PP28b	18	5.32	7.08	920.08	0.01	20.90	0.030	2.58	2.03

Table A.6. Porosity data from stained cross-sections of perpendicular bone specimens.

	Bone (Pixels)	Total (Pixels)	Porosity (%)
PP02	33547	41699	19.5%
PP03	25797	31059	16.9%
PP04	61503	68346	10.0%
PP05	69804	81977	14.8%
PP06	76844	79827	3.7%
PP07	52030	56810	8.4%
PP08	45056	50665	11.1%
PP09	43168	56322	23.4%
PP10	43379	62302	30.4%
PP12	37707	43774	13.9%
PP13	67578	74024	8.7%
PP14	66050	76634	13.8%
PP15	29341	34137	14.0%
PP16	66006	85252	22.6%
PP17	29099	33402	12.9%
PP18	87797	100901	13.0%
PP19	75149	99736	24.7%
PP20	67324	86982	22.6%
PP21	84893	105391	19.4%
PP22	76138	84575	10.0%
PP23	52362	57918	9.6%
PP24	10420	11466	9.1%
PP25	41367	45319	8.7%
PP26	36817	40503	9.1%
PP27	91413	111205	17.8%
PP28	55797	71386	21.8%
PP29	62829	72158	12.9%
PP31	109448	118586	7.7%
PP32	123319	160033	22.9%
PP33	55829	61288	8.9%
PP35	111136	139891	20.6%
PP39	236070	305571	22.7%

Table A.7. Porosity data from stained cross-sections of parallel bone specimens.

	Bone (Pixels)	Total (Pixels)	Porosity (%)
PP02	59955	74687	19.7%
PP04	23619	25450	7.2%
PP05	32821	38448	14.6%
PP06	121544	136713	11.1%
PP07	47076	51903	9.3%
PP08	72309	85020	15.0%
PP09	52524	58510	10.2%
PP10	69059	86167	19.9%
PP11	135612	168833	19.7%
PP12	68397	76470	10.6%
PP13	67312	76059	11.5%
PP14	62774	72731	13.7%
PP15	67010	77393	13.4%
PP16	50708	66943	24.3%
PP17	65382	71443	8.5%
PP18	89707	97636	8.1%
PP19	51343	65791	22.0%
PP20	112397	137864	18.5%
PP21	39143	47067	16.8%
PP22	51157	57322	10.8%
PP23	27210	29493	7.7%
PP24	12117	13427	9.8%
PP25	21753	24577	11.5%
PP27	67091	105630	36.5%
PP28	37794	42043	10.1%
PP29	72273	85481	15.5%
PP30	51137	56511	9.5%
PP32	100422	125993	20.3%
PP34	122032	141013	13.5%
PP35	146688	168171	12.8%
PP39	592119	889588	33.4%

APPENDIX B
RAW DATA FROM CHAPTER 3

Table B.1. Raw data collected from rigid interface impacts.

Specimen	Age (days)	Drop Height (cm)	Falling Mass (g)	Impact Force (N)	Displacement at Max Load (mm)	Impact Duration (s)	Failure Energy (J)	Stiffness (kN/m)	Average Thickness (mm)	Area (mm ²)
PI001	2	10	1564	447.83	3.83	0.0034	0.888	246.39	1.22	--
PI003	2	10	1564	407.78	4.74	0.0048	1.057	135.70	1.35	73.6
PI050	2	15	1564	490.18	6.83	0.0059	1.604	68.56	1.03	116.6
PI004	3	15	1919	607.74	11.91	0.0071	2.082	38.15	1.44	58.0
PI079	3	20	1669	562.13	9.00	0.0062	2.284	123.57	1.06	58.6
PI016	4	20	1669	608.82	5.70	0.0038	2.070	169.57	1.46	340.8
PI023	5	20	1669	574.48	8.53	0.0068	2.437	173.26	1.02	118.6
PI062	5	20	1669	604.21	5.40	0.0031	1.542	210.25	1.27	148.9
PI076	5	20	1669	605.84	7.10	0.0058	2.410	186.47	1.14	122.0
PI013	6	20	1919	598.37	8.98	0.0066	2.831	118.34	1.43	102.1
PI049	6	20	1669	527.10	7.68	0.0052	2.207	92.61	1.18	76.4
PI007	7	20	1669	681.99	8.67	0.0058	2.297	86.76	1.11	60.8
PI008	7	20	1919	889.95	8.49	0.0062	2.842	193.90	1.12	91.7
PI071	8	20	1669	533.75	8.78	0.0071	2.444	147.54	1.33	43.5
PI032	9	20	1669	575.02	8.66	0.0059	2.288	75.92	1.34	63.9
PI066	10	30	1669	446.88	6.94	0.0032	1.938	101.41	1.26	--
PI057	11	35	1669	786.11	10.12	0.0058	4.182	135.12	1.27	68.7
PI030	12	35	1669	725.02	10.39	0.0053	3.907	140.62	1.19	111.5
PI045	12	35	1669	793.17	8.83	0.0045	3.856	219.84	1.72	226.4
PI046	14	35	1669	805.79	7.85	0.0035	3.011	152.72	1.71	155.3
PI077	14	35	1669	648.73	8.36	0.0038	3.051	226.56	1.07	161.5

Table B.1. Continued

Specimen	Age (days)	Drop Height (cm)	Falling Mass (g)	Impact Force (N)	Displacement at Max Load (mm)	Impact Duration (s)	Failure Energy (J)	Stiffness (kN/m)	Average Thickness (mm)	Area (mm ²)
PI028	15	35	1669	852.08	9.13	0.0039	2.888	226.65	1.73	132.0
PI064	15	35	1669	811.63	5.00	0.0020	1.806	312.27	1.06	284.9
PI018	16	35	1669	812.58	8.58	0.0037	2.841	131.88	1.80	169.8
PI067	17	35	1669	696.11	5.09	0.0021	1.989	205.66	1.44	134.4
PI112	19	45	1669	965.16	9.89	0.0050	4.694	158.68	1.84	132.0
PI053	20	60	1919	882.76	13.35	0.0047	6.582	247.52	2.53	246.9
PI142	22	30	1919	728.96	6.38	0.0037	2.314	191.49	1.64	115.7
PI144	22	30	1919		8.41	0.0057	3.108	274.16	1.72	253.0
PI138	24	40	1919	830.50	4.27	0.0015	1.509	444.68	1.64	704.3
PI140	24	35	1919	835.65	7.17	0.0032	3.913	406.51	1.93	100.3
PI146	26	50	1919	1044.57	11.40	0.0043	5.392	154.78	2.14	241.8
PI148	26	80	1919	1253.48	17.18	0.0054	10.044	167.92	3.24	270.9
PI134	28	90	1919	1356.78	12.91	0.0040	6.335	176.20	3.17	254.4
PI136	28	60	1919	1404.02	12.51	0.0038	4.845	188.64	2.77	107.2
PI080	4	20	1669	Computer malfunction, data not recorded - skull damage reported						
PI010	7	20	1669	Computer malfunction, data not recorded - skull damage reported						
PI020	13	35	1669	Computer malfunction, data not recorded - skull damage reported						
PI117	35	40	2169	1202.85	6.66	0.0026	3.663	301.61	2.36	204.8
PI119	52	52	2169	2144.66	4.78	0.0013	2.114	559.05	3.17	403.0

Table B.2. Skull damage measurements for rigid interface impacts.

Specimen	Bone Fracture (mm)	Suture Damage (mm)	Total Damage (mm)
PI001	8	0	8
PI003	11	0	11
PI050	31	0	31
PI004	47	0	47
PI079	47	0	47
PI016	4	0	4
PI023	38	0	38
PI062	7	0	7
PI076	0	0	0
PI013	28	0	28
PI049	26	22	48
PI007	25	0	25
PI008	25	0	25
PI071	80	0	80
PI032	17	0	17
PI066	8	12	20
PI057	66	10	76
PI030	25	35	60
PI045	15	21	36
PI046	21	30	51
PI077	88	0	88
PI028	20	0	20
PI064	79	10	89
PI018	22	0	22
PI067	83	10	93
PI112	5	0	5
PI053	29	0	29
PI142	10	0	10
PI144	10	0	10
PI138	60	0	60
PI140	85	0	85
PI146	105	0	105
PI148	85	0	85
PI134	0	0	0
PI136	85	0	85
PI080	30	0	30
PI010	14	0	14
PI020	23	0	23

Table B.3. Raw data collected from compliant (1.1 MPa Hexcel) interface impacts.

Specimen	Age (days)	Drop Height (cm)	Falling Mass (g)	Impact Force (N)	Displacement at Max Load (mm)	Impact Duration (s)	Failure Energy (J)	Stiffness (kN/m)	Average Thickness (mm)	Area (mm ²)
PI034	2	10	1564	448.10	6.24	0.0058	1.048	81.41	1.47	100.3
PI035	2	10	1564	467.78	6.78	0.0064	1.078	122.59	1.28	288.1
PI056	2	10	1564	414.30	5.77	0.0067	1.119	105.31	1.10	146.4
PI005	3	20	1644	495.07	8.81	0.0059	2.174	61.15	1.58	85.2
PI081	3	20	1644	425.43	7.25	0.0041	1.457	79.63	1.00	245.8
PI060	4	20	1669	425.29	9.06	0.0056	1.955	75.59	0.90	25.5
PI078	4	20	1669	465.61	9.48	0.0063	2.219	96.01	1.02	90.6
PI022	5	20	1669	462.22	9.74	0.0070	2.369	62.41	0.88	196.4
PI024	5	20	1669	519.91	8.45	0.0061	2.356	77.24	1.22	104.1
PI063	5	20	1669	561.31	7.43	0.0050	2.188	92.51	0.93	121.4
PI012	6	20	1669	432.49	10.02	0.0075	2.413	70.42	1.24	74.8
PI025	6	20	1669	509.18	9.02	0.0057	2.082	88.69	1.32	85.5
PI011	7	20	1669	445.11	10.58	0.0069	2.176	74.78	1.07	98.5
PI040	7	20	1669	615.34	7.96	0.0057	2.359	95.32	0.91	184.9
PI072	8	20	1669	472.40	6.55	0.0039	1.692	161.49	1.45	308.3
PI069	9	20	1669	706.83	6.24	0.0043	2.239	187.03	1.12	334.8
PI065	10	30	1669	548.55	10.57	0.0054	3.013	81.84	1.26	87.4
PI059	11	35	1669	605.02	11.69	0.0063	4.043	101.59	1.27	148.7
PI031	12	35	1669	646.97	11.15	0.0056	3.776	110.66	1.24	134.7
PI037	12	35	1669	972.89	11.03	0.0053	3.876	170.96	1.45	419.9
PI021	13	35	1669	666.65	11.71	0.0063	4.104	110.93	1.51	247.6
PI014	14	40	1669	803.21	11.63	0.0062	4.802	140.71	1.42	378.5
PI015	14	35	1669	737.37	11.02	0.0059	4.085	208.23	1.44	328.6
PI041	14	35	1669	1020.68	9.28	0.0041	3.291	206.82	2.16	130.0

Table B.3. Continued

Specimen	Age (days)	Drop Height (cm)	Falling Mass (g)	Impact Force (N)	Displacement at Max Load (mm)	Impact Duration (s)	Failure Energy (J)	Stiffness (kN/m)	Average Thickness (mm)	Area (mm ²)
PI027	15	35	1669	1034.12	9.59	0.0044	3.560	120.62	2.13	235.7
PI029	15	35	1669	657.56	5.24	0.0020	1.098	145.00	1.23	331.1
PI052	16	35	1669	744.70	6.19	0.0025	1.942	163.92	1.72	217.8
PI082	16	35	1669	624.30	8.66	0.0040	3.184	236.86	1.22	279.5
PI068	17	35	1669	619.68	9.00	0.0039	2.714	159.61	1.37	152.6
PI054	20	60	1919	939.23	10.90	0.0034	4.188	106.85	1.91	519.5
PI143	22	30	1919	704.79	7.02	0.0046	1.521	111.32	1.59	497.8
PI145	22	30	1919	700.32	9.08	0.0054	2.745	150.64	2.70	117.0
PI139	24	40	1919	700.32	13.47	0.0058	5.300	86.238	1.34	1026.8
PI141	24	35	1919	887.92	10.91	0.0052	5.105	190.50	2.27	1437.8
PI147	26	50	1919	956.74	11.31	0.0045	5.881	171.27	1.75	706.2
PI149	26	80	1919	1169.59	17.09	0.0052	10.722	114.65	3.18	948.0
PI135	28	90	1919	1121.67	23.71	0.0069	10.712	75.14	2.54	1179.8
PI137	28	60	1919	1099.68	21.19	0.0072	8.581	94.07	2.77	401.0
PI122	33	52	2169	1097.51	11.63	0.0041	5.630	152.54	2.77	765

Table B.4. Skull damage measurements for compliant interface impacts.

Specimen	Bone Fracture (mm)	Suture Damage (mm)	Total Damage (mm)
PI034	53	0	53
PI035	117	0	117
PI056	52	0	52
PI005	112	0	112
PI081	30	0	30
PI060	9	11	20
PI078	30	0	30
PI022	57	30	87
PI024	17	20	37
PI063	36	16	52
PI012	7	14	21
PI025	34	40	74
PI011	190	0	190
PI040	78	0	78
PI072	16	0	16
PI069	11	0	11
PI065	132	0	132
PI059	129	15	144
PI031	141	0	141
PI037	0	41	41
PI021	75	0	75
PI014	103	0	103
PI015	65	22	87
PI041	12	53	65
PI027	105	0	105
PI029	95	0	95
PI052	41	0	41
PI082	50	0	50
PI068	27	10	37
PI054	23	0	23
PI143	0	0	0
PI145	0	0	0
PI139	60	0	60
PI141	0	0	0
PI147	0	0	0
PI149	40	0	40
PI135	0	0	0
PI137	0	0	0
PI122	0	0	0

MICHIGAN STATE UNIVERSITY LIBRARIES



3 1293 03062 8832